



HAL
open science

Mineral cathodic electro-precipitation and its kinetic modelling in thin-film microfluidic reactor during advanced electro-oxidation process

Faidzul Hakim Adnan, Emmanuel Mousset, Steve Pontvianne, Marie-Noëlle Pons

► To cite this version:

Faidzul Hakim Adnan, Emmanuel Mousset, Steve Pontvianne, Marie-Noëlle Pons. Mineral cathodic electro-precipitation and its kinetic modelling in thin-film microfluidic reactor during advanced electro-oxidation process. *Electrochimica Acta*, 2021, 387, pp.138487. 10.1016/j.electacta.2021.138487. hal-03429792

HAL Id: hal-03429792

<https://hal.science/hal-03429792v1>

Submitted on 15 Nov 2021

HAL is a multi-disciplinary open access archive for the deposit and dissemination of scientific research documents, whether they are published or not. The documents may come from teaching and research institutions in France or abroad, or from public or private research centers.

L'archive ouverte pluridisciplinaire **HAL**, est destinée au dépôt et à la diffusion de documents scientifiques de niveau recherche, publiés ou non, émanant des établissements d'enseignement et de recherche français ou étrangers, des laboratoires publics ou privés.



Distributed under a Creative Commons Attribution - NonCommercial - NoDerivatives 4.0 International License

1 **Mineral cathodic electro-precipitation and its kinetic modelling in**
2 **thin-film microfluidic reactor during advanced electro-oxidation**
3 **process**

4
5 Faidzul Hakim ADNAN¹, Emmanuel MOUSSET^{1,*}, Steve PONTVIANNE¹, Marie-Noëlle PONS^{1,2}

6 ¹ *Laboratoire Réactions et Génie des Procédés, Université de Lorraine, CNRS, LRGP, F-54000*
7 *Nancy, France*

8 ² *LTSER-LRGP, CNRS, Université de Lorraine, F-54000 Nancy, France*

9
10
11
12 **ACCEPTED IN**

13 ***ELECTROCHIMICA ACTA* JOURNAL**

14 ***(Special Issue from ISE Belgrade online meeting 2020 - Symposium 12)***

15 **FOR CONSIDERATION**

16
17
18 *Contact of corresponding author: emmanuel.mousset@cnrs.fr

20 **HIGHLIGHTS**

- 21 • Local cathodic alkalization occurs predominantly due to H₂O reduction not O₂
- 22
- 23 • Electromigration does not influence electro-precipitation within the conditions
- 24
- 25 • Mg(OH)₂ electro-precipitation depends only on applied current density
- 26
- 27 • Gas evolution and Mg²⁺ ion decrease CaCO₃ electro-precipitation
- 28
- 29 • Models to predict electro-precipitation in thin-film cell have been proposed

30

31

32 ABSTRACT

33 It is presented for the first time the occurrence and modelling of cathodic mineral electro-precipitation
34 in microfluidic thin-film configuration of electrochemical advanced oxidation process (EAOP), in
35 order to better understand and predict the cathode's scaling when treating water containing Mg^{2+} and
36 Ca^{2+} . Upon a systematic study, the main results show that when an inter-electrode distance of 500
37 μm is used at 4 mA cm^{-2} , local alkalization on cathode surface occurs despite the absence of dissolved
38 O_2 suggesting that it takes place due predominantly to water reduction (current efficiency $> 99\%$) and
39 not dissolved O_2 reduction. Moreover, electromigration phenomenon could be neglected when
40 varying ionic strength from 0.02 to 0.1 mol L^{-1} , while diffusion was the kinetic rate-limiting step. In
41 addition, $Ca(OH)_2$ and $MgCO_3$ precipitates were not formed under all investigated conditions.
42 $Mg(OH)_2$ electro-precipitation was found to be highly dependent on current density, but independent
43 of other ionic species jointly present in electrolyte. $Mg(OH)_2$ precipitated once interfacial pH of 10.2
44 was reached. More $CaCO_3$ was electro-precipitated at lower current density (ca. 7.2%) owing to more
45 vigorous gas evolution when higher current density was applied. 12% less $CaCO_3$ electro-
46 precipitation was found in the presence of Mg^{2+} confirming its inhibiting effect towards $CaCO_3$
47 scaling. The mathematical model proposed could fit well the experimental curves (Root mean square
48 error (RMSE) < 0.1163) and permit to predict the evolution of concentration of depositing species
49 (i.e. Mg^{2+} , Ca^{2+} and CO_3^{2-}). Furthermore, the role of hydroxyl radicals ($\cdot OH$) produced at boron-
50 doped diamond (BDD) anode could be neglected upon the applied conditions, meaning that the
51 outcome of this study is reliable across all types of water containing Mg^{2+} , Ca^{2+} and/or CO_3^{2-} in
52 compliance to their ubiquity when it is to be treated by electrolysis in general.

53 **Keywords:** advanced oxidation process, electro-oxidation, electro-precipitation, microfluidic,
54 scaling

55 **1. Introduction**

56 Occurrence of bio-recalcitrant pollutants in the effluent of municipal or industrial wastewater
57 treatment plants (WWTPs) has been raising concerns amongst different stakeholders in the field of
58 environment and ecology. More and more organic pollutants traceable in the wastewater have been
59 categorized as emerging pollutants due to their recalcitrance property and potential toxicity to living
60 organisms [1, 2]. In the objective of elimination of persistent pollutants in aquatic environment and
61 for water reuse purpose, additional treatment to the effluent of WWTPs seems obligatory. A variety
62 of supplementary treatments has been proposed across literature and the majority of them are based
63 on the fundamentals of chemical oxidation where strong oxidants are involved in the degradation of
64 pollutants. Classical processes such as chlorination, ozonation and advanced oxidation processes
65 (AOPs) (e.g. ozonation, peroxonation, heterogeneous photocatalysis and (photo)-Fenton processes)
66 are to some extent well established to degrade effectively contaminants in aqueous media [3].
67 Nevertheless, their efficiency comes with firstly high price tag [4] and secondly the prerequisite of
68 adding chemical reagents into the media to be treated.

69 Electrochemical advanced oxidation processes (EAOPs) have also been reported to remove
70 recalcitrant organic pollutants [5, 6]. A huge boost to the AOPs is that EAOPs do not necessarily
71 require the addition of chemical reagents since strong hydroxyl radical oxidants ($\cdot\text{OH}$) are
72 electrogenerated continuously in-situ [7]. Owing to the development of diamond-based anode, higher
73 degree of electrochemical oxidation of organic contaminants has been reached [8, 9]. Furthermore,
74 the application of microfluidic reactor within the framework of EAOPs has spurred the capability of
75 wastewater treatment [10-14]. It allows mineralization of organic pollutants without the addition of
76 supporting electrolyte. The micrometric inter-electrode distance vastly accommodates the
77 phenomenon of limitation by mass transfer and ohmic resistance [15] in the case of effluent having
78 relatively low ionic conductivity [16].

79 In spite of that, there is a major drawback within the application of EAOPs and more generally
80 electrolysis to treat wastewater. While treating water of varying concentrations of calcium (Ca^{2+}) and
81 magnesium (Mg^{2+}) ions), a layer of insulating deposit can be formed on the surface of cathode.
82 Despite low concentration of Ca^{2+} and Mg^{2+} in an effluent, in case of the operation of electrochemical
83 cells in continuous-mode such, most of the time, encountered in industrial applications, the deposit
84 progressively passivates the whole electrode surface. Sequencing polarity inversion might be applied
85 as counter-measure but it might take a toll on treatment efficacy, duration of operation and overall
86 operational cost. Furthermore, cathode in operation must be able to tolerate high anodic current during
87 the inverted polarization step given the fact that some cathode materials have been reported to be
88 corroded in such conditions [17]. Upon treating water with high Ca^{2+} and Mg^{2+} content, sequencing
89 inversion of polarity might not be the best strategy since the passivation of electrode occurs anyhow.
90 Eventually, without regular intervention, electrochemical cells become very inefficient or probably
91 are no longer operational.

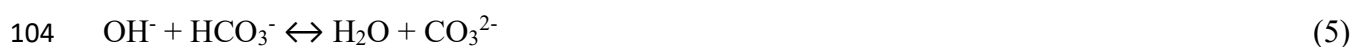
92 The mechanism of formation of deposits has been well established in the literature [18, 19]. When
93 the electrode is polarized at a sufficiently negative potential, dissolved oxygen (O_2) is reduced to
94 hydroxide ions (OH^-) according to Eq. (1), resulting in an increase of local pH [20, 21].



96 At a more cathodic potential, reduction of solvent (H_2O) can take place according to Eq. (2) which
97 also produces hydroxide ions as well as hydrogen gas (H_2).



99 As shown in Eqs. (3)-(4), in the presence of Mg^{2+} and Ca^{2+} , deposits of hydroxide can be produced.
100 Moreover, the pH increment also shifts thermodynamic ratio of carbonates/bicarbonates (Eq. (5))
101 favoring the production of carbonate scales as written in Eqs. (6)-(7).



107 Different studies have already demonstrated the formation of aforementioned deposits in
108 electrochemical cell while operating with different types of water with varying contents of Ca^{2+} and
109 Mg^{2+} . They are characterized by their source and application domain: synthetic water for cooling
110 system in cooling towers and oil refineries [22, 23], artificial [24, 25] and natural groundwater [26,
111 27], mineral potable water [28, 29], artificial [19, 30-32] and real seawater [33, 34]. Interestingly, the
112 reported works were all conducted on the classical rotating disk electrode (RDE) possessing effective
113 exposed surface area of 0.2 cm^2 [19, 24-28, 30, 33], 0.5 cm^2 [22, 23, 35], 1 cm^2 [32, 36, 37] and 1.5
114 cm^2 [31]. Either carbon steel, gold or stainless steel was used as the working electrode playing the
115 role of cathode. To the best of authors' knowledge, the study of electro-precipitation outside
116 aforementioned configuration is scarce.

117 Due to the omnipresence of calcium and magnesium in water, further study to understand and more
118 particularly to avoid the formation of insulating deposition at larger scale seems primordial. It is
119 within this context that a detailed investigation has been carried out to understand the influence of
120 electrolytic composition towards the formation of mineral deposits on electrode surface during
121 EAOP. The objective is to establish operating conditions in-which scaling does not occur, or, is
122 minimized owing to the benefits attributed by a microfluidic cell. Moreover, addition of chemical
123 reagents is no longer compulsory in micro-reactor; hence, interference possibly originating from the
124 supporting electrolyte is avoided. Magnesium hydroxide ($\text{Mg}(\text{OH})_2$), calcium carbonate (CaCO_3) and

125 magnesium carbonate (MgCO_3) deposits are studied due to the ubiquity of Mg^{2+} , Ca^{2+} and HCO_3^-
126 $/\text{CO}_3^{2-}$ ions in water sources. Results presented in this paper are the first to elucidate the phenomenon
127 of passivation in microfluidic reactor, a configuration very distinctive to those reported in the
128 literature where RDE were used as working electrode. The geometry and configuration of
129 microfluidic cell adopted in this work are closely representative to reactors used in industries.
130 Notably, the difference between electrode surface in this present study is 25 to 250 times bigger
131 compared to RDEs (0.2 to 2 cm^2) used in the literature. The present design is more adapted for further
132 applications on a larger scale. Synthetic water is used in this work, but it closely mimics the average
133 characteristic of effluent of municipal WWTPs particularly the concentration of Ca^{2+} , Mg^{2+} and
134 carbonates as well as pH and ionic conductivity. Furthermore, it is the first time that the influence on
135 electro-precipitation of hydroxyl radicals produced at high O_2 evolution overvoltage anode is studied.
136 Novel theoretical models are developed in this paper where the objectives are two-fold; first,
137 assumptions made to establish the models lead to a better understanding of the mechanism of mineral
138 electro-precipitation if they occur. Second, these models are the first to be reported to predict the
139 evolution of electro-precipitating ions, particularly under the configuration of thin-film microfluidic
140 reactor.

141 **2. Experimental**

142 **2.1 Chemicals**

143 Calcium sulfate dihydrate (>90%), magnesium sulfate heptahydrate (>98%), sodium
144 hydrogenocarbonate (>99.5%) and sodium sulfate (>97%) were purchased from VWR International
145 (Fontenay-sous-Bois, France). Sulfuric acid (95-97%) was obtained from Sigma Aldrich (Saint-
146 Quentin-Fallavier, France). Sodium hydroxide (1 N) was provided by Honeywell Fluka (Seelze,
147 Germany). Titanium (IV) oxysulfate-sulfuric acid (27-31%) solution for hydrogen peroxide (H_2O_2)
148 detection was purchased from Sigma Aldrich (Saint-Quentin-Fallavier, France). These chemical
149 reagents were used as purchased without further treatment.

150 **2.2 Preparation of electrolyte**

151 Electrolyte with and without carbonates contained sources of Ca^{2+} (150 mg L^{-1}) and Mg^{2+} (5 mg L^{-1})
152 dissolved in ultrapure water ($18.2 \text{ M}\Omega \text{ cm}$) provided by PureLab ELGA Classic water purification
153 system (Veolia Water, Antony, France). Electrolyte with carbonates contained a concentration of 60
154 mg-C L^{-1} . Initial values of pH and ionic conductivity were always adjusted to 7.6 and $1000 \mu\text{S cm}^{-1}$
155 respectively. A small quantity of sodium sulfate (1.4 to 5 mmol L^{-1}) was added when required in order
156 to reach a constant ionic conductivity and strength (0.02 mol L^{-1}) for suitable comparison. The
157 artificial WWTP effluent properties are representative to the average characteristics of effluent from
158 the outlet of municipal WWTPs.

159 **2.3 Electrochemical system**

160 The effluent (0.5 L) to be treated was stored in a double-jacket stainless steel reservoir connected to
161 a thermostatic bath in order to ensure a working temperature of 25°C (Bioblock Scientific,
162 PolyScience, Niles, IL, USA). A peristaltic pump (Masterflex, Cole-Parmer, Vernon Hills, IL, USA)
163 was used to circulate the solution. pH (Mettler Toledo InPro 4260i) and conductivity (Mettler Toledo
164 InPro 7100i) were measured at regular time. The electrochemical cell was similar to the one described
165 in previous work [16]. It consisted of a planar-electrodes filter-press type cell. Its body was made on-
166 site and made of poly(methyl methacrylate) (PMMA). The material is chemically and thermally
167 resistant in the applied operating conditions. Rubber seals were designed, built-in, to provide tightness
168 and avoid leakage. Planar electrodes were used as anode and cathode. Double-sided boron-doped
169 diamond (BDD) coated on Niobium (Nb) substrate (DiaCCon, Fürth, Germany) or Platinum plate
170 (Ögussa, Vienna, Austria) with 50 cm^2 effective surface area each were used as anode. Stainless steel
171 (Gantois Industries, Saint-Dié-des-Vosges, France) with the same effective surface area (50 cm^2) was
172 used as cathode. Prior to utilization, stainless steel was preconditioned chemically by soaking it in
173 sulfuric acid solution of 0.25 M . Non-conducting spacer made of polytetrafluoroethylene (PTFE)
174 (Bohlender, Grünsfeld, Germany) was placed in-between to avoid contact between anode and

175 cathode. This spacer with micrometric thickness of 500 μm was used across this work, hence defining
176 inter-electrode distance of electrochemical cell. Electrolysis was carried out using a power supply
177 HMP4040 (Rohde & Schwarz, Meudon-la-Forêt, France). The influence of two sufficiently different
178 regions of current density were investigated in this work, i.e. 0.4 and 4 mA cm^{-2} . The latter was
179 selected because it has been defined as optimal current density from previous work where similar
180 reactor setting was used to degrade pharmaceutical pollutants [16]. All experiments were carried out
181 at least in duplicate to ensure reproducibility.

182 In preliminary experiments, two blank solutions were used. One composed of only sulfates (6.65
183 mmol L^{-1}) and another one containing carbonates at 60 mg-C L^{-1} with Na_2SO_4 (5 mmol L^{-1}) as
184 supporting electrolyte. Both blank electrolytes possessed similar initial pH value (7.6) and ionic
185 strength of 0.02 mol L^{-1} . Under another preliminary study where an absence of dissolved O_2 was
186 sought for the entire experiment, effluent in reservoir was bubbled with nitrogen gas (N_2) while it
187 was recirculating through the pilot initiating from 30 min before electrolysis until the end of
188 experiment. 500 μm inter-electrode distance and the highest current density condition (4 mA cm^{-2})
189 were implemented for preliminary experiments.

190 **2.4 Analytical methods**

191 Evolutions of Ca and Mg elements concentration were monitored, after filtering the samples using
192 Phenex 0.45 μm filter (Phenomenex, Le Pecq, France), via inductively coupled plasma optical
193 emission spectroscopy (ICP-OES) Thermo iCAP 6000 (Thermo Fisher, Illkirch-Graffenstaden,
194 France). The calibration was performed according to PlasmaCAL Custom Standard method (SCP
195 Sciences) using a certified multi-element solution (1000 mg L^{-1} , SCP Sciences, Villebon-sur-Yvette,
196 France). Ca and Mg elements measured by ICP-OES were assimilated to Ca^{2+} and Mg^{2+} when
197 dissolved in solution.

198 The concentration of sulfate (SO_4^{2-}) was measured using ionic chromatography Dionex ICS 6000
199 (Thermo Fisher, Noisy-Le-Grand, France). Its calibration curve was obtained from a series of
200 different known concentration of SO_4^{2-} prepared from a standard solution of $1000 \mu\text{g mL}^{-1}$. The anion
201 exchange column IC DionexTM IonPacTM AS18 (Thermo Fisher, Noisy-Le-Grand, France) equipped
202 with a column guard was used. The column was kept at 23°C . An aliquot of $15 \mu\text{L}$ of sample was
203 injected passing through the column. The temperature of samples tray was maintained at 20°C . The
204 ICS 6000 was equipped with a conductivity detector for detection system and it was kept constant at
205 35°C . The mobile phase rate was set at 1 mL min^{-1} .

206 Total inorganic carbon (TIC) was measured using a TOC-meter V_{CSH} TC/TN (Shimadzu, Marne-La-
207 Vallée, France). A TIC standard solution of $1000 \mu\text{g mL}^{-1}$ (TechLab, Metz, France) was used for
208 calibration and control.

209 Hydrogen peroxide (H_2O_2) concentration was measured via complexing $\text{H}_2\text{O}_2\text{-Ti}^{4+}$ method [38]. UV-
210 2600 spectrophotometer (Shimadzu, Marne-La-Vallée, France) was used to detect maximum
211 absorbance of the complex at 410 nm wavelength. H_2O_2 concentration was deduced according to the
212 Beer-Lambert law from a calibration curve established with the use of standard H_2O_2 solutions.

213 Linear scan voltammetry (LSV), chrono-amperometry and chrono-potentiometry were performed
214 using a potentiostat (Ametek, Massy, France) connected to the designed electrochemical cell. The
215 electrode potential was reported against saturated silver chloride reference electrode (V/SSCE) in this
216 work.

217 **2.5 Recovery step of Ca and Mg elements**

218 The purpose of this step was to support the monitoring of the evolution of Ca and Mg concentrations
219 in the electrolyte using ICP-OES. It was assumed that if they decreased in solution over time, they
220 partook in deposition reactions and took solid form. The recovery of Ca and Mg from the solid form
221 could assert where the majority of the deposition reactions took place, if they occurred. The recovery

222 process was carried out using a solution of sulfuric acid at 0.25 M. The objective was to decrease the
223 pH to re-dissolve the deposits into ionic form. Once completely dissolved, the acid solution was
224 filtered through Phenex 0.45 μm filter (Phenomenex, Le Pecq, France) and was analyzed by ICP-
225 OES to determine the Ca and Mg concentrations. To ensure a thorough recovery of cations that might
226 undergo scaling in different compartment of experimental pilot, the recovery step was performed on
227 cathode, anode as well as pilot tubing. Hence, knowing the initial and final concentration of cations
228 in the electrolyte, mass balance of cations could be performed to observe the distribution of deposition
229 formed in and out of the electrochemical reactor in addition to attesting a quasi-complete recovery of
230 cations.

231 Theorem of conservation of mass tells that the sum of mass i element (Ca and Mg) recovered at
232 different compartment of experimental pilot at the end of experiment should be equal to the initial
233 mass of i present in electrolyte before the electrolysis, if there is no loss in the closed system. Mass
234 balance and percentage recovery of i are then defined in [Eq. \(8\)](#) and [Eq. \(9\)](#), respectively:

$$235 \quad m_{recovered} = m_{f,elec} + m_{anode} + m_{cathode} + m_{tube} \quad (8)$$

$$236 \quad \left(m_{recovered} / m_{i,elec} \right) \times 100 = \% recovery \quad (9)$$

237 where $m_{recovered}$ is the total mass (in mg) of i recovered from different compartment, $m_{i,elec}$ the
238 initial mass of i element in electrolyte before electrolysis, $m_{f,elec}$ the mass of i that remains in
239 electrolyte at the end of electrolysis, m_{anode} the mass of i recovered from the surface of anode,
240 $m_{cathode}$ the mass of i recovered from the surface of cathode and m_{tube} the mass of i recovered from
241 the surface of tubing of pilot.

242 **3. Modelling**

243 **3.1 Electrolyte containing Mg^{2+} and Ca^{2+}**

244 Mg^{2+} and Ca^{2+} react with OH^- to produce precipitates of $Mg(OH)_2$ and $Ca(OH)_2$ when the product of
 245 concentrations of both cations with OH^- exceeds the constants of solubility of $Mg(OH)_2$ ($K_{S,Mg(OH)_2}$)
 246 ($K_{S,Mg(OH)_2} = 5.61 \times 10^{-12}$ [39, 40]) and of $Ca(OH)_2$ ($K_{S,Ca(OH)_2}$) ($K_{S,Ca(OH)_2} = 5.00 \times 10^{-6}$ [39, 40])
 247 respectively. Knowing Mg^{2+} and Ca^{2+} concentrations in the system, the concentration of OH^- at which
 248 its product reaches the $K_{S,Mg(OH)_2}$ and $K_{S,Ca(OH)_2}$ values, respectively, can be calculated. It is noted
 249 as critical OH^- concentration (OH^-_{crit}).

250 During the electrolysis, OH^- ions are produced on cathode by reduction of either dissolved O_2 via 4-
 251 electrons reaction (Eq. (1)) and/or water via 2-electrons reaction (Eq. (2)). Since both reactions took
 252 place in parallel on cathode in our system under the applied current densities, they have been
 253 considered as competing reactions. CE_{O_2} and CE_{H_2O} terms were used to proportionate the current
 254 efficiency as a result of the reduction of O_2 and H_2O respectively. The rate of production of OH^-
 255 (r_{OH^-}) on cathode in batch mode can thus be written as in Eq. (10):

$$256 \quad r_{OH^-} = + \frac{d[OH^-]}{dt} = \frac{\nu_{O_2} j_{app}}{n_{O_2} F} CE_{O_2} + \frac{\alpha \nu_{H_2O} j_{app}}{n_{H_2O} F} CE_{H_2O} \quad (10)$$

257 where ν_{O_2} and ν_{H_2O} are the stoichiometry coefficient of OH^- via reaction of reduction of O_2 (Eq. (1))
 258 and H_2O (Eq. (2)) respectively, while n_{O_2} and n_{H_2O} are their number of electrons involved in those
 259 faradaic reactions, j_{app} is the applied current density in $mA\ cm^{-2}$ and F is the Faraday constant ($96,485$
 260 $C\ mol^{-1}$). α is a corrective term ($\alpha < 1$) assigned to the faradaic production of OH^- which occurs
 261 concomitantly with physical evolution of gas bubbles on cathode surface at high applied current
 262 density. In accordance to Eq. (2), H_2 gas also evolves when H_2O is reduced to OH^- . H_2 gas evolution
 263 is more intense when higher current density value is used, according to the Faraday's law. Gas
 264 evolution on cathode surface contributes to two major consequences; firstly, less surface area could
 265 be available for mineral deposition on cathode surface [41]. Secondly, it could promote detachment
 266 of deposits occurring on the electrode [42, 43].

267 On the surface of cathode, OH⁻ ions are produced abundantly and continuously. Water is the solvent
 268 of electrolyte thus its electrochemical reduction is limitless. Meanwhile, dissolved O₂ are not only
 269 consumed on cathode (Eq. (1)), but it is also concomitantly produced on anode through water
 270 oxidation (Eq. (11)).



272 In microfluidic configuration, the distance between cathode and anode is very small thus the
 273 replenishment of dissolved O₂ could take place continuously [44]. As a result, once OH⁻_{crit} is reached,
 274 OH⁻ concentration is considered constant and it does not vary whilst reacting with Mg²⁺ and Ca²⁺
 275 because the concentration of OH⁻ is significantly larger and in excess compared to the cations
 276 concentrations. In addition, it is assumed that Mg²⁺ and Ca²⁺ were not reduced or oxidized by direct
 277 electrochemical reduction or oxidation, so that their oxidation state remained constant all along the
 278 electrolysis [45].

279 Hence, according to Eqs. (3)-(4), the rate of reaction of Mg²⁺ and Ca²⁺ can be written according to
 280 Eq. (12) and Eq. (13) respectively:

$$281 \quad r_{Mg^{2+}} = -r_{Mg(OH)_2} = -k_{Mg(OH)_2}[Mg^{2+}][OH^-]^2 \quad (12)$$

$$282 \quad r_{Ca^{2+}} = -r_{Ca(OH)_2} = -k_{Ca(OH)_2}[Ca^{2+}][OH^-]^2 \quad (13)$$

283 where $k_{Mg(OH)_2}$ and $k_{Ca(OH)_2}$ are the third order rate constants regarding the reaction of precipitation
 284 of Mg(OH)₂ and Ca(OH)₂ respectively in L² mol⁻² s⁻¹, while [Mg²⁺], [Ca²⁺] and [OH⁻] are the molar
 285 concentration (in mol L⁻¹) of Mg²⁺, Ca²⁺ and OH⁻ ions, respectively.

286 3.2 Electrolyte containing Ca²⁺ and CO₃²⁻

287 Ca²⁺ reacts with CO₃²⁻ to form CaCO₃ precipitates when the product of concentrations of both ions
 288 exceeds the constant of solubility of CaCO₃ ($K_{S,CaCO_3}$) ($K_{S,CaCO_3} = 3.36 \times 10^{-9}$ [40, 46-48]).

289 Supersaturation degree (S) of CaCO₃ is defined in **Eq. (14)** and follows by its supersaturation index
290 in **Eq. (15)** [49, 50].

$$291 \quad S = \frac{[Ca^{2+}][CO_3^{2-}]}{K_{sp,CaCO_3}} \quad (14)$$

$$292 \quad SI = \log_{10}(S) \quad (15)$$

293 Thermodynamically, CaCO₃ can precipitate when $S > 1$ (or $SI > 0$). Carbonates concentration can be
294 estimated from TIC measurement that corresponds to the sum of all forms of inorganic carbon (**Eq.**
295 **(16)**):

$$296 \quad TIC = [H_2CO_3] + [HCO_3^-] + [CO_3^{2-}] \quad (16)$$

297 where H_2CO_3 is carbonic acid and HCO_3^- is bicarbonate ion.

298 The inorganic carbon species are linked together by acidity constants K_{a1} and K_{a2} given in **Eqs. (17)**–
299 **(18)**, respectively.

$$300 \quad K_{a1} = \frac{[H^+][HCO_3^-]}{[H_2CO_3]} \quad (17)$$

$$301 \quad K_{a2} = \frac{[H^+][CO_3^{2-}]}{[HCO_3^-]} \quad (18)$$

302 Their ratios are therefore governed by the solution pH. pK_{a1} and pK_{a2} values are 6.3 and 10.4 [51],
303 respectively. Under the range of our pH operating conditions and at the proximity of cathode surface,
304 the quantity of H_2CO_3 is negligible and the expression of TIC can be simplified into **Eq. (19)**.

$$305 \quad TIC = [HCO_3^-] + [CO_3^{2-}] \quad (19)$$

306 CO_3^{2-} concentration is related to the concentration of OH^- produced on cathode surface by its
307 equilibrium with HCO_3^- in agreement with **Eq. (5)** and **Eq. (18)**. Hence, the evolution of interfacial

308 CO_3^{2-} concentration ($[\text{CO}_3^{2-}]_{int,t}$) can be estimated from TIC values by combining **Eqs. (10), (18)**
 309 and **(19)** giving out an expression in **Eq. (20)**.

$$310 \quad [\text{CO}_3^{2-}]_{int,t} = \frac{K_{a2} \times \text{TIC}_t}{\frac{K_W}{[\text{OH}^-]_t} + K_{a2}} \quad (20)$$

311 where K_{a2} and the concentration of interfacial CO_3^{2-} , OH^- and TIC are expressed in mol L^{-1} while the
 312 equilibrium constant of auto-ionization of water (K_W) is considered equaled to 10^{-14} at 25°C .

313 According to **Eq. (6)**, the rate of reaction of Ca^{2+} and CO_3^{2-} producing CaCO_3 can be defined as
 314 indicated in **Eq. (21)**:

$$315 \quad r_{\text{Ca}^{2+}} = r_{\text{CO}_3^{2-}} = -r_{\text{CaCO}_3} = -k_{\text{CaCO}_3} [\text{Ca}^{2+}][\text{CO}_3^{2-}]_{int} \quad (21)$$

316 where k_{CaCO_3} is the second order rate constant (in $\text{L mol}^{-1} \text{s}^{-1}$) regarding the reaction of precipitation
 317 of CaCO_3 . Identically to the $\text{Mg}^{2+}/\text{Ca}^{2+}$ system (section **3.1**), OH^- accumulates at the vicinity of
 318 cathode during the electrolysis.

319 **3.3 Electrolyte containing Mg^{2+} and CO_3^{2-}**

320 In absence of Ca^{2+} , Mg^{2+} can precipitate in the form of $\text{Mg}(\text{OH})_2$ upon reaching OH^-_{crit} as well as
 321 MgCO_3 when the product of concentrations of Mg^{2+} and CO_3^{2-} exceeds thermodynamic solubility
 322 constant of MgCO_3 (K_{S,MgCO_3}) ($K_{S,\text{MgCO}_3} = 1.59 \times 10^{-8}$ **[52]**). Local alkalization remains valid at the
 323 surface of cathode. Knowing the fact that Mg^{2+} could participate in the precipitation reactions of
 324 $\text{Mg}(\text{OH})_2$ and MgCO_3 , on top of kinetic law defined in **Eq. (12)**, the rate of reaction of Mg^{2+} can be
 325 rewritten in **Eq. (22)** as follow:

$$326 \quad r_{\text{Mg}^{2+}} = -r_{\text{Mg}(\text{OH})_2} - r_{\text{MgCO}_3} = -k_{\text{Mg}(\text{OH})_2} [\text{Mg}^{2+}][\text{OH}^-]^2 - k_{\text{MgCO}_3} [\text{Mg}^{2+}][\text{CO}_3^{2-}] \quad (22)$$

327 where k_{MgCO_3} is the second order rate constant (in $\text{L mol}^{-1} \text{s}^{-1}$) regarding the reaction of precipitation
 328 of MgCO_3 .

329 3.4 Electrolyte containing Mg²⁺, Ca²⁺ and CO₃²⁻

330 In the matrix of electrolyte containing Mg²⁺, Ca²⁺ and CO₃²⁻, both Mg²⁺ and Ca²⁺ can undergo
331 precipitation in accordance to **Eqs. (3)-(4)** and **Eqs. (6)-(7)**. The phenomenon of local alkalization
332 remains accurate in this system.

333 In the presence of Mg²⁺, depositing MgOH₂ consumes OH⁻ over time. The cathodic production of
334 OH⁻ in **Eq. (10)** is modified taking into account this event as indicated in **Eq. (23)**:

$$335 \quad r_{OH^-} = + \frac{d[OH^-]}{dt} = \frac{\nu_{O_2} j_{app}}{n_{O_2} F} CE_{O_2} + \frac{\alpha \nu_{H_2O} j_{app}}{n_{H_2O} F} CE_{H_2O} - 2 k_{Mg(OH)_2} [Mg^{2+}][OH^-]^2 \quad (23)$$

336 3.5. Modelling software and fitting evaluation

337 Aquasim **[53]** was used to model the evolution of Mg²⁺, Ca²⁺ and CO₃²⁻. The fitting between
338 experimental data and theoretical model was evaluated using root mean square error (RMSE), model
339 efficiency (ME) and index of agreement (IOA) according to **Eq. (24)**, **Eq. (25)** and **Eq. (26)**,
340 respectively **[54]**:

$$341 \quad RMSE = \sqrt{\frac{\sum_{i=1}^K (y_i - y'_i)^2}{K}} \quad (24)$$

$$342 \quad ME = 1 - \frac{\sum_{i=1}^K (y_i - y'_i)^2}{\sum_{i=1}^K (y_i - y_M)^2} \quad (25)$$

$$343 \quad IOA = 1 - \frac{\sum_{i=1}^K (y_i - y'_i)^2}{\sum_{i=1}^K (|y'_i - y_M| + |y_i - y_M|)^2} \quad (26)$$

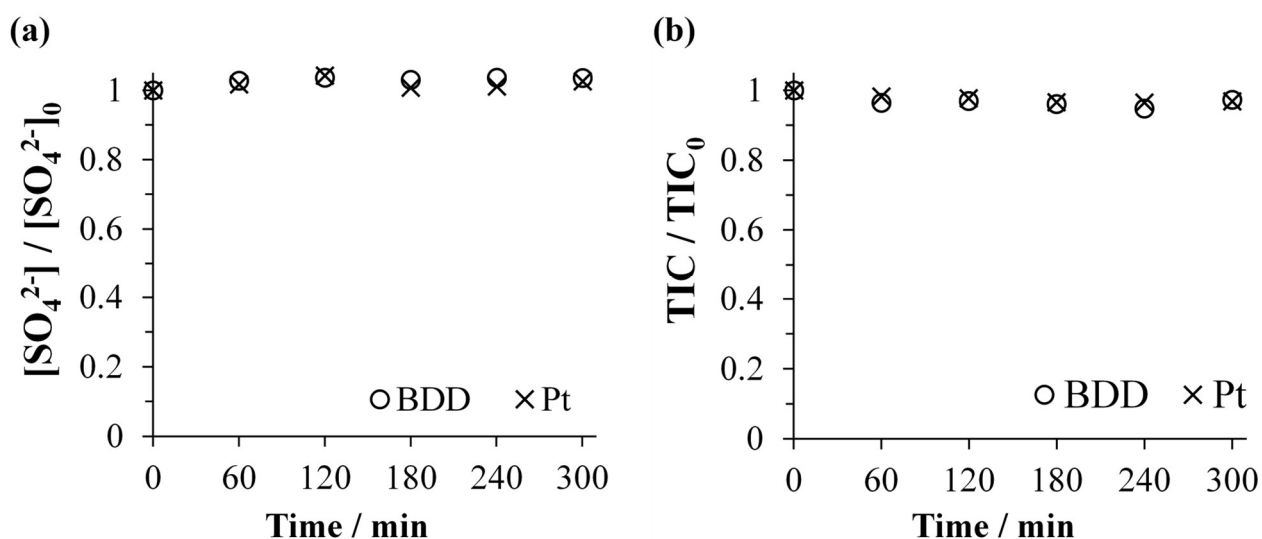
344 where K is the number of steps of checked values, y'_i is the experimental value, y_i is the corresponding
345 simulated value and y_M is the average of simulated value.

346 4. Results and discussion

347 4.1 Stability of anions in blank solutions using BDD or Pt anode

348 Preliminary experiments were conducted in the microfluidic reactor to check on the behavior of
349 anions (SO_4^{2-} and $\text{HCO}_3^-/\text{CO}_3^{2-}$) during electro-oxidation in the absence of depositing elements. BDD
350 and Pt anodes were used to verify the involvement of $\cdot\text{OH}$ towards any oxidation of anions. The
351 former is well-known for its high overpotential for oxygen evolution reaction (OER). Consequently,
352 physi-sorbed $\cdot\text{OH}$ are produced at anode vicinity [55, 56]. Contrastingly, the overpotential for OER
353 with Pt anode is low. Thus $\cdot\text{OH}$ is chemi-sorbed on the anode surface, making the radical not available
354 [57].

355 The evolution of concentration of SO_4^{2-} and TIC are depicted in Fig. 1. It has been noticed that the
356 concentration of both anions remained constant throughout the entire electro-oxidation experiments
357 whether BDD or Pt was used as anode. First deduction that can be made is that SO_4^{2-} and HCO_3^-
358 $/\text{CO}_3^{2-}$ anions were stable during the electro-oxidation process whatever the anode employed. It
359 means that they will not interfere if there is occurrence of electro-precipitation on cathode surface.
360 Secondly, under these applied conditions, the formation of oxidizing agent of $\cdot\text{OH}$ did not inflict
361 towards the degradation of SO_4^{2-} and $\text{HCO}_3^-/\text{CO}_3^{2-}$ anions. Anode potential was measured to be +2.40
362 V/SSCE (or +2.60 V/SHE), which already hit the standard potential of formation of $\cdot\text{OH}$ when 4 mA
363 cm^{-2} is applied. The oxidation conditions were not strong enough to oxidize SO_4^{2-} into
364 peroxydisulfates ($\text{S}_2\text{O}_8^{2-}$) [58] and CO_3^{2-} into peroxydicarbonates ($\text{C}_2\text{O}_6^{2-}$) [59, 60] with $\text{SO}_4^{\cdot-}$ and
365 $\text{CO}_3^{\cdot-}$ as intermediates, respectively. Moreover, anion of strong acid such as SO_4^{2-} is very unlikely to
366 form complex with alkaline-earth cations such as Ca^{2+} and Mg^{2+} [61]. In overall, $\cdot\text{OH}$ involvement
367 in microfluidic reactor set-up did not lead to the oxidation of SO_4^{2-} and $\text{HCO}_3^-/\text{CO}_3^{2-}$ anions in blank
368 electrolytes during electro-oxidation experiments. In overall, the presence of $\cdot\text{OH}$ in our applied
369 microfluidic reactor conditions could thus be omitted from the developed theoretical models and was
370 confirmed further in the next sections.



371

372 **Fig. 1.** Evolution of concentration of (a) SO_4^{2-} (in blank solution containing sulfates only) and (b)
 373 TIC (in blank solution containing carbonates only) during the electrolysis of blank solutions using
 374 BDD (○) or Pt (×) as anode. Cathode: stainless steel, ionic strength of both blank solutions: 0.02
 375 mol L⁻¹, applied current density: 4 mA cm⁻² and inter-electrode distance: 500 μm.

376 **4.2 Local alkalization on cathode surface: reactions' selectivity between reduction of dissolved**
 377 **O₂ and water**

378 According to **Eq. (1)** and **Eq. (2)** respectively, both dissolved O₂ and H₂O can undergo faradaic
 379 reduction generating OH⁻ (**Eq. (10)**). To identify the weight of contribution of dissolved O₂ to produce
 380 OH⁻ with respect to local alkalization phenomenon, tests in presence and absence of dissolved O₂
 381 were conducted. Under the investigated micrometric distance, anodic activity might be involved in
 382 this selectivity, since H₂O could be also oxidized to O₂.

383 **Fig. 2** plots the evolution of concentration of Mg²⁺, Ca²⁺ and TIC in the experiments with and without
 384 dissolved O₂. In both cases, the concentration of all species decreased regardless of presence of
 385 dissolved O₂. This indicates that the initial presence of dissolved O₂ was insignificant towards the
 386 phenomenon of local alkalization, and consequently towards the formation of deposits on cathode
 387 surface. Notably from **Fig. 2(a)** and **Fig. 2(b)**, it has been deduced that the source of OH⁻ ions came
 388 mainly from reduction of water and not from dissolved O₂. A slight decrease in the electro-

389 precipitation of Ca^{2+} in absence of dissolved O_2 was due to slightly lesser amount of OH^- participating
390 in thermodynamic shift of $\text{HCO}_3^-/\text{CO}_3^{2-}$ towards the formation of CO_3^{2-} (**Fig. 2(b)**). Thus, lesser
391 extent of CaCO_3 electro-precipitation was observed.

392 Under these setups, the concentration of electrogenerated H_2O_2 was measured to further study the
393 contribution of dissolved O_2 reduction producing OH^- ions in accordance with **Eq. (27)**.



395 The H_2O_2 production was found to be very small (maximum concentration went up to $1.8 \mu\text{mol L}^{-1}$,
396 data not shown), whatever the applied current density. Most of H_2O_2 concentration values fell below
397 the limit of quantification of the method, determined to be $0.8 \mu\text{mol L}^{-1}$. This observation was
398 attributed to the low H_2 evolution overvoltage on stainless steel cathode [62]. Similar poor production
399 of H_2O_2 on stainless steel cathode was reported by Sopaj et al. [38]. They measured approximately
400 $40 \mu\text{mol L}^{-1}$ of H_2O_2 under their experimental setup when 4.8 mA cm^{-2} was applied [38]. Unlike the
401 configuration presented in our work, compressed air was continuously bubbled under their
402 experimental setup to supply dissolved O_2 to promote the Fenton reaction, which explains the
403 difference in measured H_2O_2 concentration.

404 CE_{O_2} and $CE_{\text{H}_2\text{O}}$ in **Eq. (10)** and **Eq. (23)** were estimated via **Eqs. (28)-(29)** at each value of current
405 density investigated in this work. Their values are tabulated in **Table 1**. The calculations are attached
406 as **Text S1** in supplementary materials.

$$407 \quad CE_{\text{O}_2} = \frac{n_{e^-} F N_{\text{O}_2}}{J_{\text{app}} t} \quad (28)$$

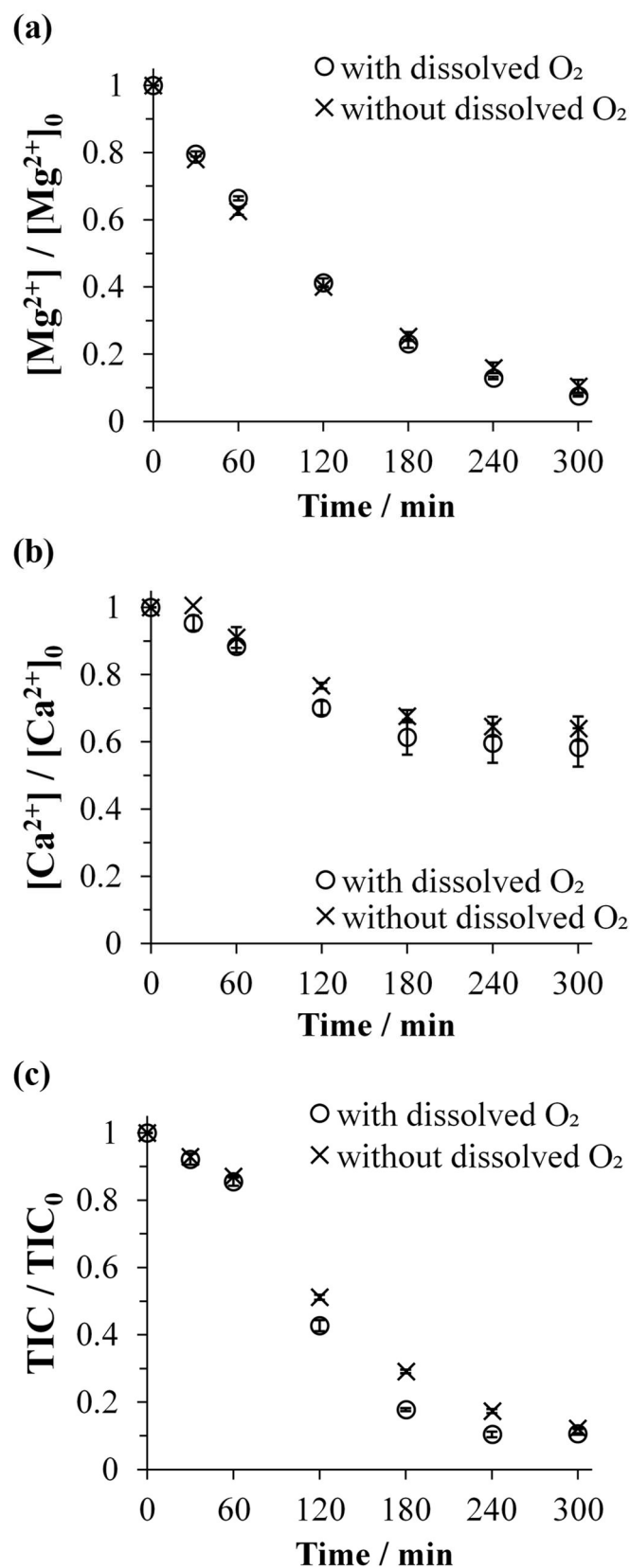
$$408 \quad CE_{\text{H}_2\text{O}} = 1 - CE_{\text{O}_2} \quad (29)$$

409 where n_{e^-} is the number of electron exchanged in **Eq. (27)**, N_{O_2} is the quantity of dissolved O_2 (in
410 mol) reduced to H_2O_2 in **Eq. (27)**, J_{app} is the applied current (in A) and t is the electrolysis time.

411 **Table 1.** Estimation of CE_{O_2} and CE_{H_2O} in faradaic production of OH^- on cathode.

$j_{app} / \text{mA cm}^{-2}$	$N_{O_2} / \mu\text{mol}$	$CE_{O_2} / \%$	$CE_{H_2O} / \%$
0.4	0.6	0.16	99.84
4	0.9	0.02	99.98

412 To conclude, local alkalization on cathode surface principally occurred due to the reduction of H_2O
413 with only slight involvement of dissolved O_2 under our experimental setup. The latter was
414 electrocatalytically reduced to OH^- with negligible production of H_2O_2 on stainless steel. Our
415 proposed model takes into consideration this observed selectivity given by higher faradaic yield of
416 CE_{H_2O} in producing OH^- as deduced in **Table 1** when applied to **Eq. (10)** and **Eq. (23)**.



417

418

419

420

Fig. 2. Evolution of concentration of **(a)** Mg^{2+} , **(b)** Ca^{2+} and **(c)** TIC during the electrolysis of artificial effluent containing 150 mg L^{-1} of Ca^{2+} , 5 mg L^{-1} of Mg^{2+} and 60 mg-C L^{-1} of $\text{HCO}_3^-/\text{CO}_3^{2-}$ in absence (×) (via bubbling with N_2 gas) and presence (○) of dissolved O_2 throughout the

421 experiment. Anode: BDD, cathode: stainless steel, applied current density: 4 mA cm⁻² and inter-
422 electrode distance: 500 μm.

423 4.3 Influence of electromigration of ionic species

424 Although calcium and magnesium deposits are formed on the surface of cathode during electrolysis,
425 Ca²⁺ and Mg²⁺ do not participate in direct electron transfer to yield Ca metal (Ca(s)) and Mg metal
426 (Mg(s)) respectively. The reduction of Ca²⁺ and Mg²⁺ each by two electrons need to overcome a
427 strong thermodynamic barrier ($E_{Ca^{2+}/Ca(s)}^0 = -2.84$ V/SHE and $E_{Mg^{2+}/Mg(s)}^0 = -2.356$ V/SHE [63]), and
428 these strong reduction conditions are not involved in the present study (cathode potential determined
429 to be -1.34 V/SHE). Instead, they reacted chemically with respective counter-ions on the surface of
430 cathode, producing scaling when solubility constant of precipitates was achieved. Despite not being
431 electroactive elements in regard to driving force of potential difference across electrochemical
432 reactor, Ca²⁺ and Mg²⁺ mobility towards cathode surface might be involved in the displacement of
433 ionic species jointly present in the bulk. In agreement with the Nernst-Planck equation, Ca²⁺ and Mg²⁺
434 were transported by forced convection thanks to electrolyte flow in-between electrodes. Under
435 stationary conditions, they underwent diffusion from electrolyte bulk through finite boundary layer
436 (i.e. diffusion layer), towards reactive zone at the proximity of cathode surface. Then through
437 migration, they were mobilized to fulfill electro-neutrality on cathode surface as the consequence of
438 local alkalization [64-66]. The two current densities investigated in this study were both above the
439 initial limiting current density (determined to be 0.25 mA cm⁻² using j_{lim} calculation [67, 68] (Text
440 S2), which was then confirmed with limiting current density plateau on linear scan voltammogram
441 (Fig. S1)) for aforementioned electrochemical cell setup while producing OH⁻. Hence,
442 electrochemical reactions taking place on the surface of cathode were considered limited by the mass
443 transport.

444 Therefore, in this section, under constant hydrodynamic parameters, the influence of electromigration
 445 of ionic species was investigated by varying the ionic strength of artificial effluent using Na₂SO₄ as
 446 supporting electrolyte. **Table 2** summarizes the values of ionic transference number for the different
 447 cases. They were calculated using **Eqs. (30)-(31) [69]** under the assumption that our electrolytic
 448 system complied with the restriction of infinite dilution where interaction between ions was not
 449 occurring.

$$450 \quad t_i = \frac{z_i C_i u_i}{\sum_i z_i C_i u_i} \quad (30)$$

451 with

$$452 \quad u_i = \frac{\lambda_i}{z_i F} \quad (31)$$

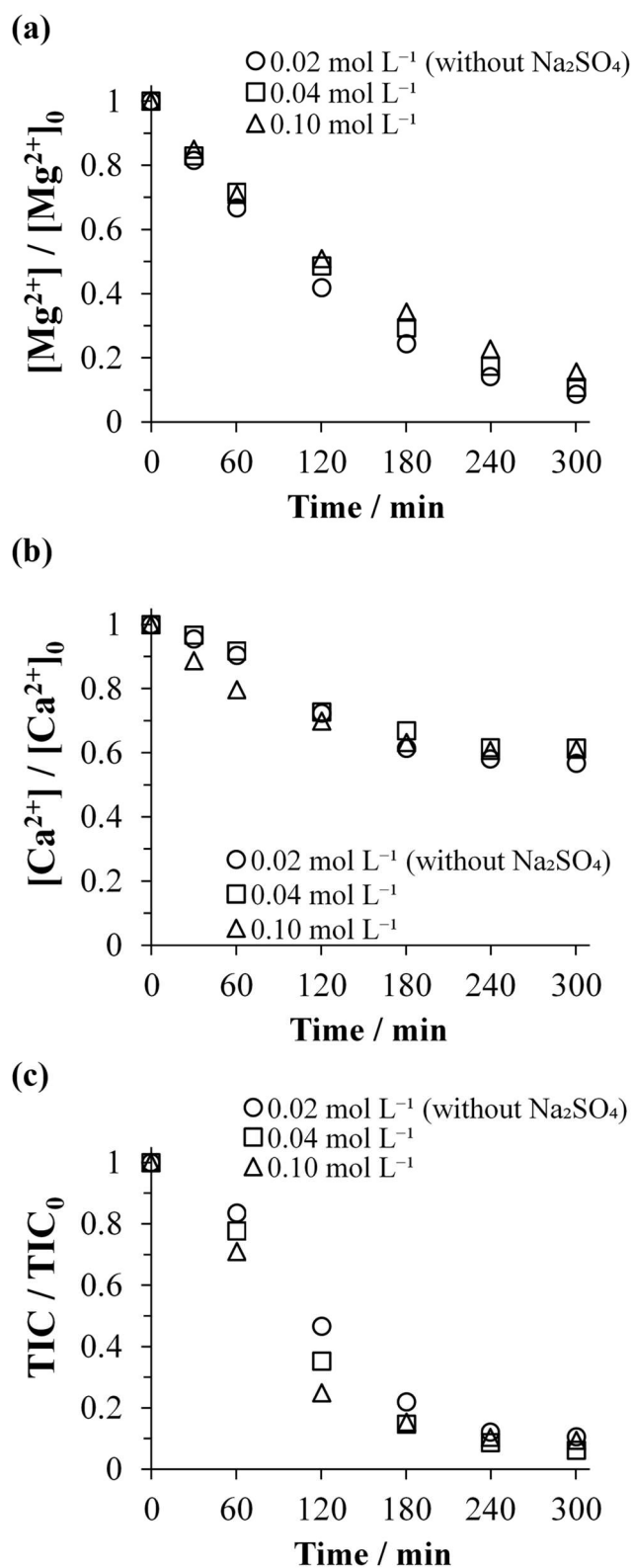
453 where t_i is the transference number, z_i the ionic charges, u_i the ionic mobility (in m² s⁻¹ V⁻¹), C_i the
 454 molar concentrations of ionic species (in mol L⁻¹) and λ_i the ionic molar conductivity (in S m² mol⁻¹).
 455 1).

456 **Table 2.** Ionic transference number for artificial effluent containing 150 mg L⁻¹ of Ca²⁺, 5 mg L⁻¹ of
 457 Mg²⁺ and 60 mg-C L⁻¹ of TIC without and with addition of Na₂SO₄ at different concentrations.

Ionic strength / mol L ⁻¹	Ionic transference number				
	Ca ²⁺	Mg ²⁺	Na ⁺	HCO ₃ ⁻	SO ₄ ²⁻
0.02 (without Na ₂ SO ₄)	0.218	0.011	0.123	0.339	0.309
0.04	0.120	0.006	0.241	0.187	0.447
0.10	0.050	0.002	0.325	0.077	0.545

458 As can be seen from **Table 2**, the more Na₂SO₄ was added to increase the ionic strength of artificial
459 effluent, the more ionic mobility of Ca²⁺, Mg²⁺ and HCO₃⁻/CO₃²⁻ were minimized by increasing
460 transport activity of Na²⁺ and SO₄²⁻.

461 **Fig. 3** depicts the trend of evolution of concentration of Mg²⁺, Ca²⁺ and TIC when the investigated
462 artificial effluent had different ionic strengths. The concentration of each ion decreased over time
463 regardless of value of ionic strength. It seemed to have very little impact on the variation of the
464 concentration of Ca²⁺ and TIC as previously suggested by Tlili et al., where migration might play
465 some role with respect to only more concentrated species in the system [64]. Standard deviations
466 were calculated between results obtained with the electrolytes with enhanced ionic mobility in
467 comparison to the one without supporting electrolyte. The average values are listed in **Table S1**. The
468 two highest deviation were obtained in Mg²⁺ and TIC concentration with evaluated deviation as low
469 as 0.049 and 0.042, respectively. Therefore, the ionic strength of electrolyte had minor effect within
470 the range of studied electrolyte concentrations towards the occurring mineral deposition on cathode
471 surface. Electromigration of ionic species other than Ca²⁺, Mg²⁺ and HCO₃⁻/CO₃²⁻ did not influence
472 the mobility of the precipitating elements in-between electrodes inside microfluidic electrochemical
473 reactor. Mass transport by diffusion was then the rate-limiting factor. Based on these results, the effect
474 of electromigration could be omitted from the theoretical model proposed in section 3. The addition
475 of small quantity of supporting electrolyte (from 1.4 to 5 mmol L⁻¹) to achieve constant ionic strength
476 across different investigated matrices of electrolyte will not influence the kinetics of mineral electro-
477 precipitation in experimental results presented onwards.



478

479 **Fig. 3.** Evolution of concentration of (a) Mg^{2+} , (b) Ca^{2+} and (c) TIC during the electrolysis of
 480 artificial effluents bearing different ionic strengths of 0.02 (○) (without the addition of supporting
 481 electrolyte), 0.04 (□) and 0.10 (△) mol L⁻¹. Anode: BDD, cathode: stainless steel, applied current
 482 density: 4 mA cm⁻² and inter-electrode distance: 500 μm.

483 4.4 Influence of matrix of electrolyte

484 4.4.1 Influence of CO_3^{2-} towards the mineral electro-precipitation

485 Electrolysis of electrolyte containing Mg^{2+} and Ca^{2+} , in presence and absence of CO_3^{2-} , in the
486 microfluidic flow-by reactor were carried out by applying 0.4 and 4 mA cm^{-2} and the results are
487 plotted in **Fig. 4** and **Fig. 5**. From **Fig. 4**, it could firstly be observed that Ca^{2+} did not precipitate in
488 the electrolyte without carbonate at both current densities. It precipitated only in presence of
489 carbonate. Thus, it has been concluded that $\text{Ca}(\text{OH})_2$ was not produced throughout these series of
490 experiment and Ca^{2+} only electro-precipitated to form CaCO_3 . This observation can be supported by
491 the value of thermodynamic constant of solubility of $\text{Ca}(\text{OH})_2$ that is high (5.00×10^{-6} [39, 40]) - thus
492 highly soluble -, hence the interfacial pH never reached the $\text{OH}^-_{\text{crit}}$ (i.e. 36.6 mol m^{-3} , $\text{pH} = 12.6$) to
493 precipitate with Ca^{2+} . Secondly, according to **Fig. 5**, Mg^{2+} only precipitated at 4 mA cm^{-2} and no
494 Mg^{2+} -based deposition occurred at 0.4 mA cm^{-2} . At low current density, since no decrease of Mg^{2+}
495 was observed, it can be concluded that $\text{Mg}(\text{OH})_2$ was not electro-precipitated. Same remark was given
496 by Deslouis et al. [30] where they did not observe precipitation of $\text{Mg}(\text{OH})_2$ when interfacial pH of
497 9.3 was not yet reached. Our result tells that there was a plateau at 4 mA cm^{-2} at the very beginning
498 of electrolysis up to 7 min before Mg^{2+} started to deposit forming $\text{Mg}(\text{OH})_2$, as soon as $\text{OH}^-_{\text{crit}}$ (0.16
499 mol m^{-3} , interfacial $\text{pH} = 10.2$) was reached (**Fig. 5**). Then, during the first hour of electrolysis at 4
500 mA cm^{-2} , a slightly higher kinetics of $\text{Mg}(\text{OH})_2$ deposition was observed in the electrolyte without
501 carbonate. In the presence of CO_3^{2-} , there was perhaps a weak competition between $\text{Mg}(\text{OH})_2$ and
502 CaCO_3 for active site on the surface of cathode [36, 70]. However, it was not accounted for MgCO_3 ,
503 otherwise the kinetics of precipitation with the electrolyte containing CO_3^{2-} would be faster and not
504 slower than the one without CO_3^{2-} . To conclude, Mg^{2+} electro-precipitated independently with regard
505 to carbonate ions.

506 Moreover, it can be seen in **Fig. 4** that CaCO_3 was already deposited at low current density, unlike
507 $\text{Mg}(\text{OH})_2$ even though the thermodynamic constant of solubility of $\text{Mg}(\text{OH})_2$ is lower than that of

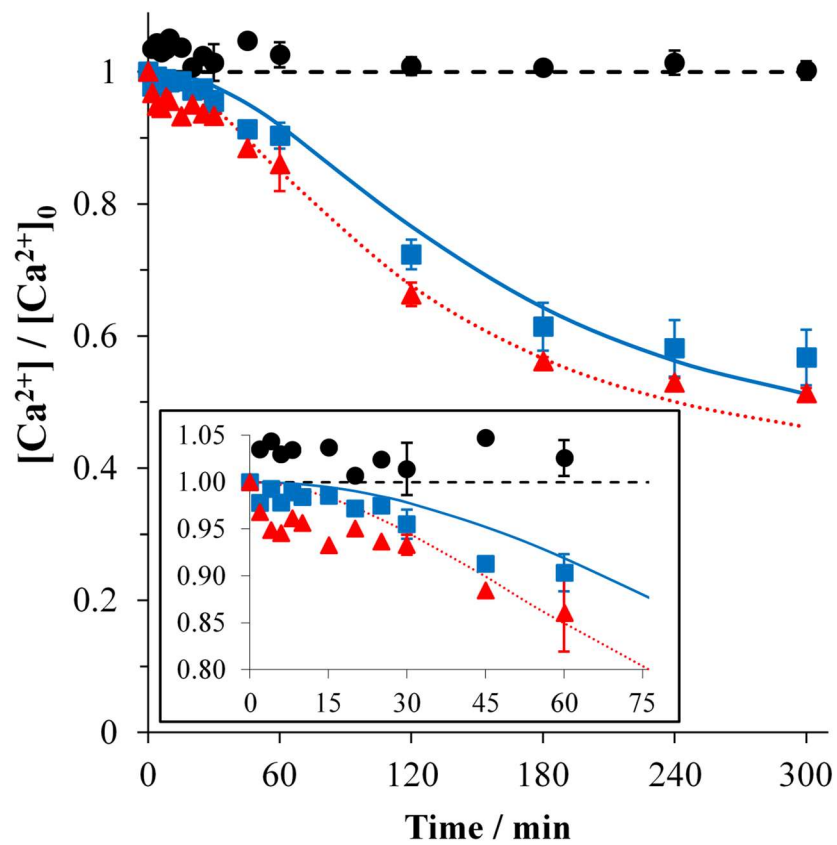
508 CaCO₃. Similar observation was reported by Okstad et al. [71]. The higher initial concentration of
509 Ca²⁺ - implemented to simulate the composition of reclaimed wastewater from urban WWTPs - can
510 be one of the reasons of this observation, whereby supersaturation degree was already high. On top
511 of that, experimental results showed that 7.2% more CaCO₃ deposition occurred at 0.4 mA cm⁻² in
512 comparison to higher applied current density of 4 mA cm⁻². To our understanding, once CaCO₃
513 electro-precipitation started to occur, it took place regardless of applied current density as long as the
514 current density was equal or higher than the starting point of the nucleation of CaCO₃ crystal. In case
515 of low and high applied current densities investigated in this work, CaCO₃ already formed at the low
516 current density (0.4 mA cm⁻²). It would behave similarly at higher applied current density except that
517 within the latter, oxidation and reduction of solvent on the surface of electrodes were occurring at
518 higher rates leading to higher amount of electro-generated gas. Given the fact that at 0.4 mA cm⁻² it
519 was already exceeding the limiting current density (0.25 mA cm⁻², see section 4.3), gas production
520 was therefore occurring at both applied conditions. It means that the influence of gas evolution was
521 taking place concomitantly with the electro-precipitation on cathode surface [72], but in an antagonist
522 way according to the level of gas production. At 0.4 mA cm⁻², the lower evolution of gas on the
523 surface of electrode could enhance the mass transfer of reactive towards the electrodes [73-76]. This
524 enhancement would be attributed to firstly micro-convection, even at small value of current density
525 [73], due to evolving and departing gas bubbles from the electrode surface. Secondly, forced
526 convection or macro-convection owing to movement and displacement of bubbles over the electrode
527 surface could also occur [74-76]. Therefore, transport of Ca²⁺ and Mg²⁺ towards cathode surface for
528 precipitation reaction were enhanced at the low current density condition. This could explain why
529 slightly more CaCO₃ was obtained at lower current density. Contrastingly, higher intensity of gas
530 evolution is expected over the surface of cathode at high applied current density (4 mA cm⁻²).
531 Therefore, bubble coverage at the electrode surface should have increased as described by Vogt et al.
532 [41]. Therefore, the more intense gas evolution at higher applied current density could have disturbed

533 the layer of CaCO₃ nuclei and in-parallel promoted the detachment of CaCO₃ deposit [42, 43, 62].
534 Consequently, less electro-precipitation of CaCO₃ was observed at higher applied current density.

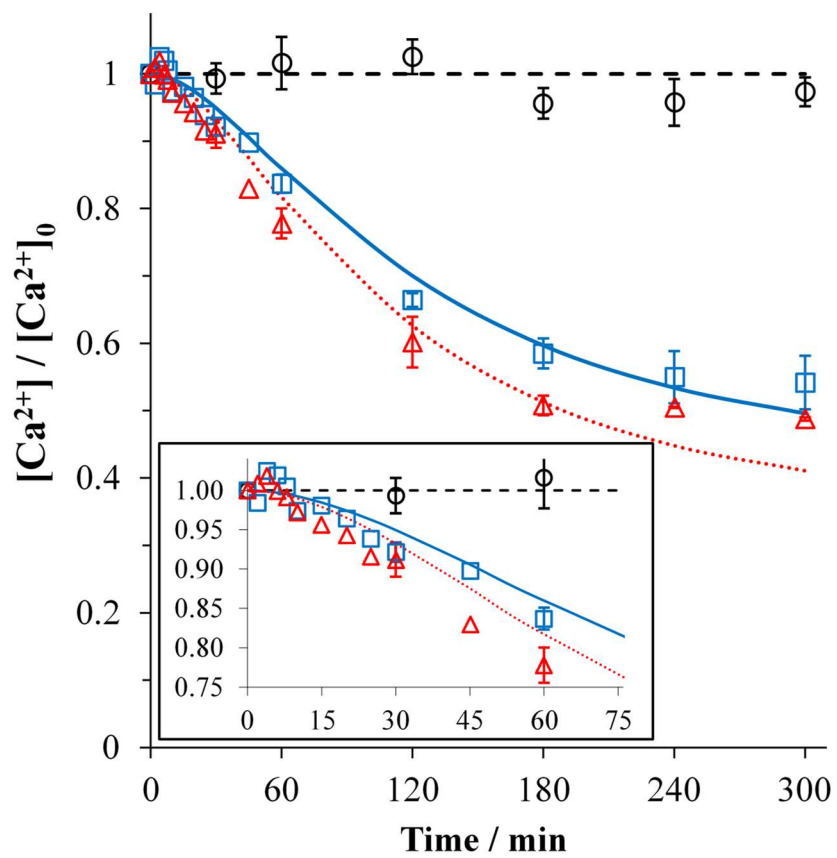
535 Furthermore, in presence of Ca²⁺ (150 mg L⁻¹) and carbonates (TIC of 60 mg-C L⁻¹), supersaturation
536 index (SI) defined in Eq. (15) equaled to 0.89 in the initial electrolyte. It means that Ca²⁺ and CO₃²⁻
537 concentrations in the bulk were already above their equilibrium state in water (where SI = 0) initially
538 [49]. From the thermodynamic point of view, CaCO₃ precipitation in the bulk and scaling on metal
539 substrate could occur. However, the induction time for homogenous and heterogeneous CaCO₃
540 nucleation varies in function of physico-chemical component of bulk liquid as well as metal substrate
541 [29, 50, 77]. According to Gabrielli et al., thermodynamics requires a 40-fold supersaturation before
542 the precipitation in the bulk can be observed, i.e. equivalent to SI value around 1.6 [18, 77, 78]. It has
543 also been demonstrated that under low supersaturation conditions, very long induction time (12 h)
544 was required before observing scaling on metal substrate [79]. This might be one of the reasons
545 sluggish kinetics of electro-precipitation of CaCO₃ was observed at the very beginning of electrolysis
546 in Fig. 4. With respect to the evolution of experimental TIC concentrations (Fig. S2 (a-d)) as well as
547 to the modeled interfacial CO₃²⁻ concentrations illustrated in Fig. 6, this slow initial kinetics were
548 also noticed. From Fig. 6, it can be noticed that on cathode surface, CO₃²⁻ departed from its initial
549 bulk concentration and rapidly increased owing to electrogenerated OH⁻ once the electrolysis started.
550 With increasing quantity of interfacial CO₃²⁻, more CO₃²⁻ was readily available to react with Ca²⁺ to
551 form CaCO₃ scaling. The supersaturation degree quickly increased, thus promoting the deposition of
552 CaCO₃. The concentration of interfacial CO₃²⁻ kept increasing as long as the rate of production of
553 OH⁻ was superior to the rate of production of CaCO₃ (or CO₃²⁻ consumption at the interface). During
554 this period, more CO₃²⁻ was shifted from HCO₃⁻ form since the OH⁻ concentration also increased, the
555 phenomenon that contributed towards local alkalization. A peak was attained when the rate of OH⁻
556 production equaled that of CO₃²⁻ consumed. Beyond this peak, the rate of electro-precipitation of
557 CaCO₃ declined due to decreasing concentration of both Ca²⁺ and CO₃²⁻ in the electrolyte at later
558 stage of electrolysis as can be observed in Fig. 4. When comparing the evolution of interfacial CO₃²⁻

559 concentration modeled at 4 mA cm^{-2} (**Fig. 6(a)**) against 0.4 mA cm^{-2} (**Fig. 6(b)**), three remarks can
560 be made; firstly, longer time was needed to reach the peak at $r_{\text{OH}^-} = r_{\text{CaCO}_3}$. Secondly, smaller
561 concentration of interfacial CO_3^{2-} was produced at higher current density and thirdly, CaCO_3 electro-
562 precipitation occurred at relatively slower rate after the peak of equivalence. The involvement of gas
563 evolution might explain the described behaviors. As above-mentioned, intensified evolving H_2 gas
564 on cathode surface at higher applied current density decreased significantly the effective surface area
565 of cathode even though the OH^- production was enhanced in the meantime. Consequently, longer
566 buffer time was observed in **Fig. 4(a)** (**inset** curve) at the beginning of electrolysis in comparison to
567 **Fig. 4(b)**. Lesser amount of interfacial CO_3^{2-} was also expected at the proximity of cathode surface
568 due to the intervention of evolving gas. This disturbance on cathode took place throughout the
569 electrolysis and consequently, plausible detachment of CaCO_3 scaling occurred along the way. In
570 overall, slower kinetics of CaCO_3 deposition was observed under high current density, affirmed by
571 the trend depicted in **Fig. 4**.

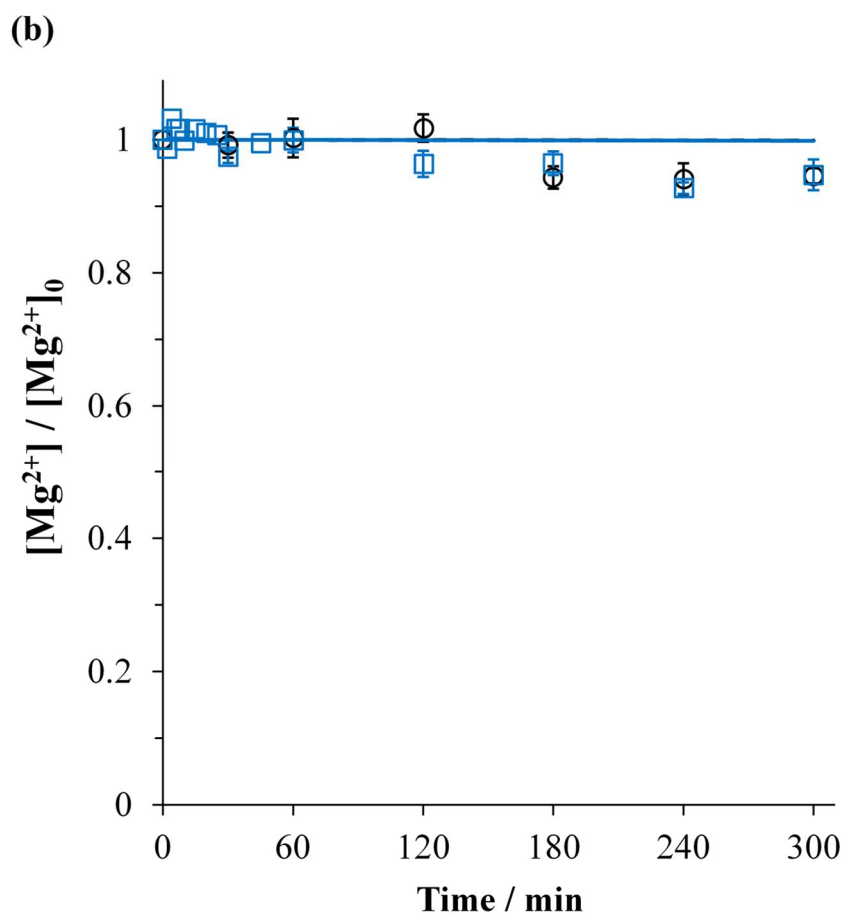
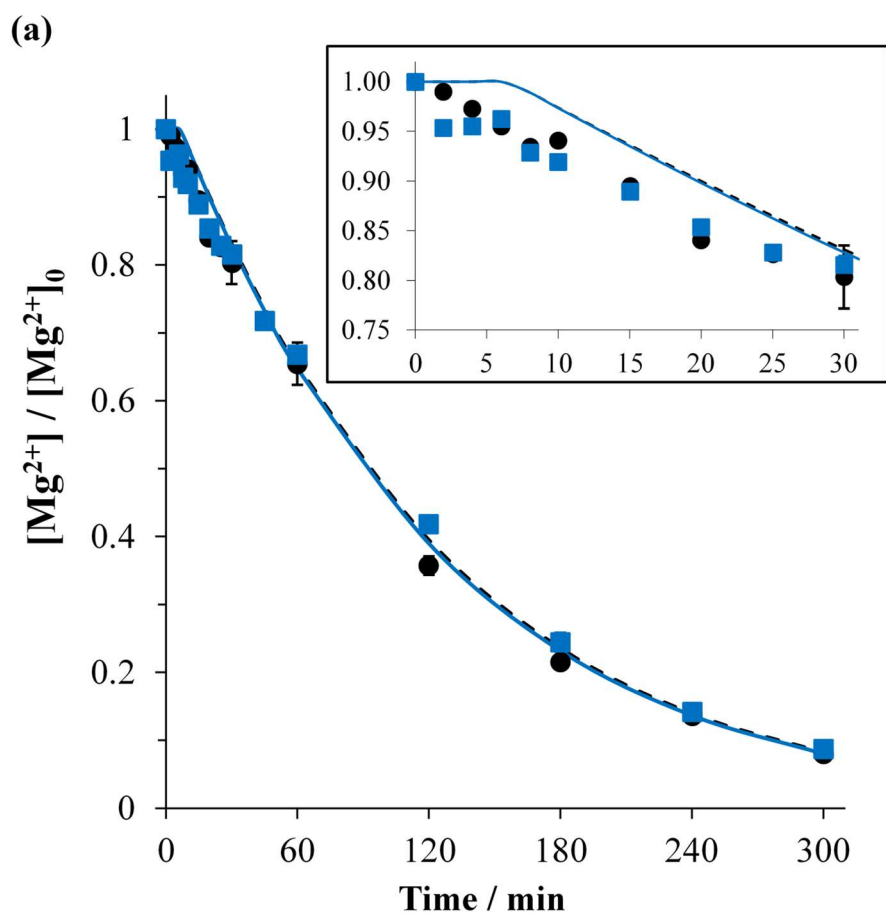
(a)



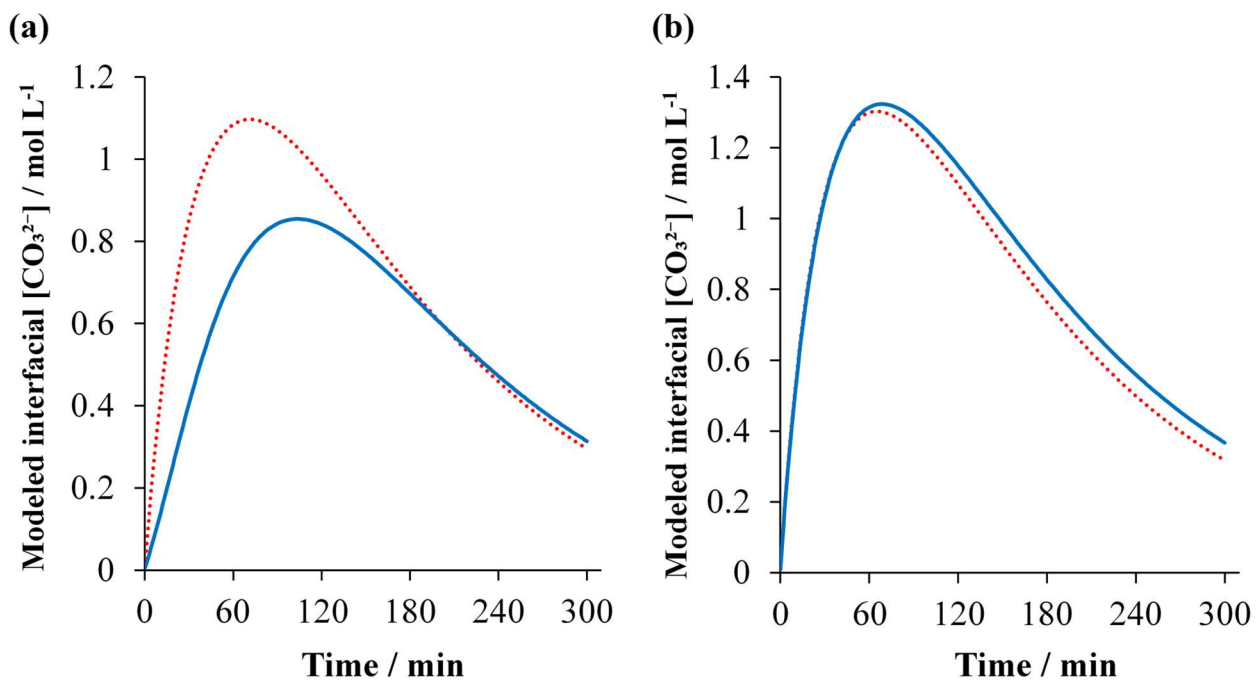
(b)



573 **Fig. 4.** Evolution of concentration of Ca^{2+} during the electrolysis of different matrices of electrolyte
574 (\bullet, \circ : Ca^{2+} and Mg^{2+} without CO_3^{2-} , \blacksquare, \square : Ca^{2+} , Mg^{2+} and CO_3^{2-} and $\blacktriangle, \triangle$: Ca^{2+} and CO_3^{2-} without
575 Mg^{2+}) at **(a)** 4 mA cm^{-2} ($\bullet, \blacksquare, \blacktriangle$) and **(b)** 0.4 mA cm^{-2} ($\circ, \square, \triangle$) applied current density. (---):
576 model curve for Ca^{2+} and Mg^{2+} electrolyte without CO_3^{2-} , (—): model curve for Ca^{2+} , Mg^{2+} and
577 CO_3^{2-} electrolyte and (.....): model curve for Ca^{2+} and CO_3^{2-} without Mg^{2+} electrolyte. **Inset:**
578 zoom of the initial kinetic evolution of Ca^{2+} . Anode: BDD, cathode: stainless steel and inter-
579 electrode distance: $500 \mu\text{m}$.



581 **Fig. 5.** Evolution of concentration of Mg^{2+} during the electrolysis of different matrices of electrolyte
 582 (\bullet , \circ : Ca^{2+} and Mg^{2+} without CO_3^{2-} and \blacksquare , \square : Ca^{2+} , Mg^{2+} and CO_3^{2-}) at (a) 4 mA cm^{-2} (\bullet , \blacksquare) and
 583 (b) 0.4 mA cm^{-2} (\circ , \square) applied current density. (—): model curve for Ca^{2+} and Mg^{2+} electrolyte
 584 without CO_3^{2-} and (—): model curve for Ca^{2+} , Mg^{2+} and CO_3^{2-} electrolyte. **Inset:** zoom of the
 585 initial kinetic evolution of Mg^{2+} . Anode: BDD, cathode: stainless steel and inter-electrode distance:
 586 $500 \mu\text{m}$.



587
 588 **Fig. 6.** Modeled concentration of interfacial CO_3^{2-} during the electrolysis of electrolyte containing
 589 Ca^{2+} , Mg^{2+} and CO_3^{2-} (—) and electrolyte containing: Ca^{2+} and CO_3^{2-} without Mg^{2+} (.....)
 590 under the polarization of (a) 4 mA cm^{-2} and (b) 0.4 mA cm^{-2} applied current density. Anode: BDD,
 591 cathode: stainless steel and inter-electrode distance: $500 \mu\text{m}$.

592 4.4.2 Influence of Mg^{2+} towards the mineral electro-precipitation

593 To investigate the role of Mg^{2+} towards CaCO_3 deposition in microfluidic reactor, two electrolytes,
 594 both consisting of Ca^{2+} and CO_3^{2-} but only one contained Mg^{2+} , were compared. According to **Fig. 4**,
 595 at both applied current densities, concentrations of Ca^{2+} decreased over time. In both cases, higher
 596 degree of CaCO_3 electro-precipitation (12%) was observed in the system in absence of Mg^{2+} . This

597 difference was even more significant when the electrochemical cell was polarized with lower current
598 density where the interface was less perturbed by evolving gas (**Fig. 4(b)**). This finding can be
599 attributed to the inhibition effect of Mg^{2+} during $CaCO_3$ deposition [25, 30, 34, 42, 49]. Mg^{2+} can
600 either incorporate into the $CaCO_3$ lattices lowering their growth kinetics on cathode surface [25, 49,
601 80], or, a thin layer of magnesian gel-like film [42, 70, 81] - which was formed prior to the $CaCO_3$
602 deposition [37, 81] - partially limited the surface reactivity of cathode towards the scaling of $CaCO_3$.
603 Nonetheless, it has been reported that $CaCO_3$ crystal can still develop and grow on the layer of
604 $Mg(OH)_2$ as confirmed by mixture of brucite and aragonite crystals from microscopic techniques [42,
605 81-83]. With regard to the competing reaction of gas evolution on the surface of cathode at higher
606 current density, it remained true while working with electrolyte without Mg^{2+} . More intense H_2 gas
607 evolution led to less $CaCO_3$ electro-precipitation (**Fig. 4**) as previously described. A slight difference
608 was found in terms of $CaCO_3$ crystallography according to literature. When cathode potential was
609 relatively low in the region of solvent reduction, $CaCO_3$ deposit has been reported to crystallize under
610 cubic calcite allotropy. Whilst in presence of Mg^{2+} , $CaCO_3$ takes aragonite form [18, 23, 37, 42, 62].
611 Under strong evolving gas activity, porous structure of $CaCO_3$ deposit has been reported [35-37, 43,
612 84].

613 In addition, the trends of modeled interfacial CO_3^{2-} depicted on **Fig. 6** complement the deduction
614 made on the inhibiting role of Mg^{2+} towards $CaCO_3$ electro-precipitation. At higher applied current
615 density (4 mA cm^{-2} , **Fig. 6(a)**), $Mg(OH)_2$ deposit was formed in the electrolyte containing Mg^{2+} . The
616 formation of $Mg(OH)_2$ deposit partly consumed interfacial OH^- . As a result, r_{OH^-} decreased as
617 accounted in the model (**Eq. (23)**). Together with H_2 gas evolution at higher current polarization, the
618 increment of interfacial CO_3^{2-} concentration was slower in the electrolyte in presence of Mg^{2+}
619 relatively to the one without Mg^{2+} . Smaller interfacial CO_3^{2-} concentration was expected at cathode
620 surface therefore lowering kinetic rate of $CaCO_3$ electro-precipitation. Contrastingly, $Mg(OH)_2$
621 electro-precipitation did not take place at lower current density. Gas evolution was significantly lower
622 at 0.4 mA cm^{-2} . Consequently, the evolution of modeled interfacial CO_3^{2-} concentrations (**Fig. 6(b)**)

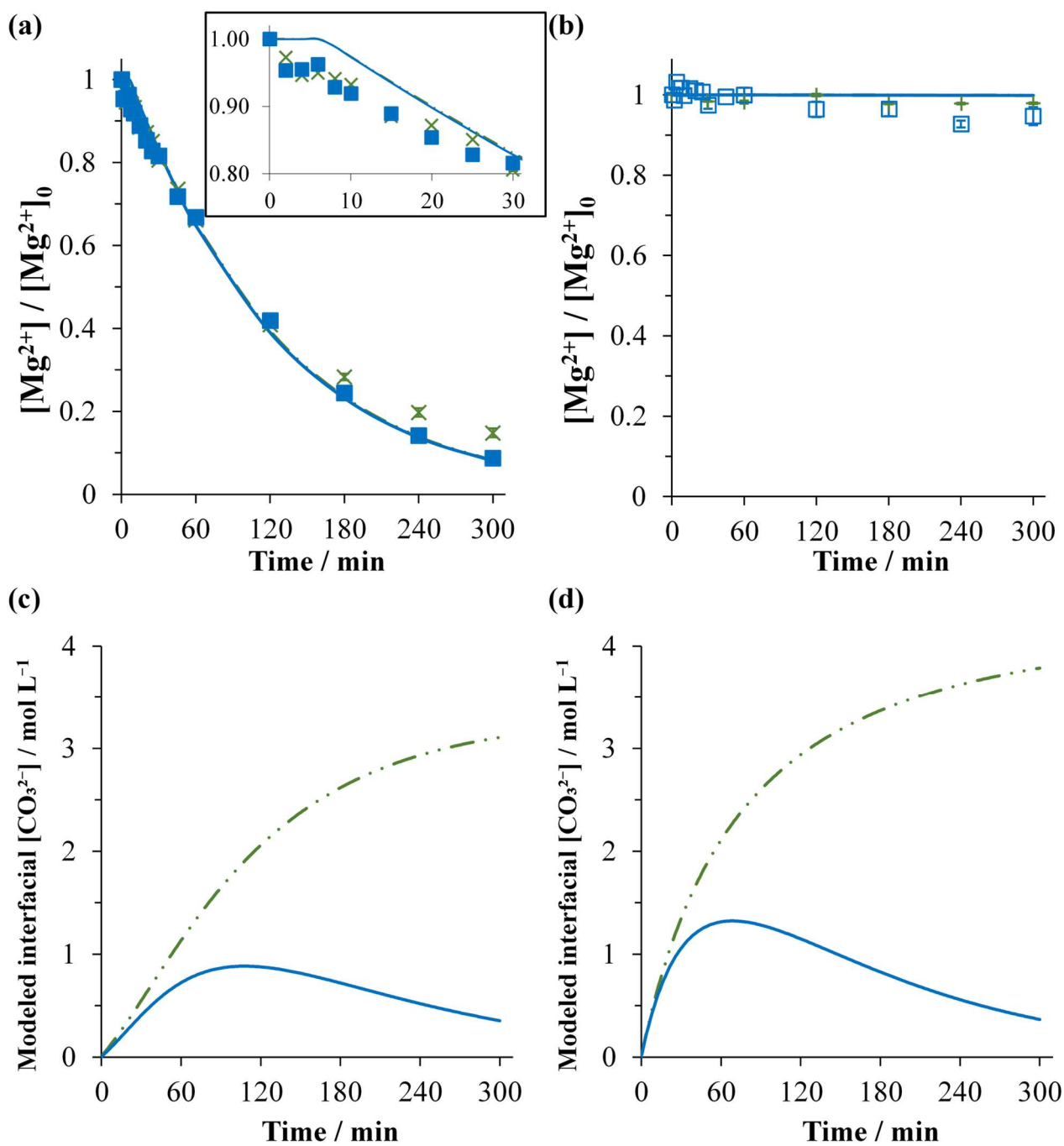
623 for both electrolytes in absence and presence of Mg^{2+} were quite similar. It means that the availability
624 of interfacial CO_3^{2-} on cathode surface was about the same for either electrolyte. Hence, it was then
625 confirmed from **Fig. 4(b)** that the lower growth rate of $CaCO_3$ deposition obtained in the presence of
626 Mg^{2+} at lower current density was due to the decrease of supersaturation degree of $CaCO_3$ in the
627 presence of Mg^{2+} [85]. As previously discussed, it can adsorb or incorporate into $CaCO_3$ crystal lattice
628 inhibiting its growth during the electrolysis [49, 80].

629 **4.4.3 Influence of Ca^{2+} towards the mineral electro-precipitation**

630 **Fig. 7** illustrates the behavior of mineral deposition during electrolysis in the presence or absence of
631 Ca^{2+} at 4 and 0.4 mA cm⁻². From **Fig. 7(a)**, it was observed that Mg^{2+} underwent electro-precipitation
632 independently of Ca^{2+} . The evolution of concentration of Mg^{2+} in presence of Ca^{2+} followed exactly
633 the trend given in absence of Ca^{2+} . This observation indicated indifferent role of Ca^{2+} towards the
634 deposition of Mg^{2+} . From **Fig. 7(b)**, it was noticed that Mg^{2+} did not precipitate at lower applied
635 current density (0.4 mA cm⁻²) in both matrices of electrolyte. The evolution of TIC in **Fig. S2(e-f)**
636 suggested that the concentration of CO_3^{2-} declined negligibly over time in the matrix without Ca^{2+}
637 relatively to the behavior in the presence of Ca^{2+} . This tendency coupled with the observation made
638 in **Fig. 7(a)** allowed deducing on the absence of electro-precipitation of $MgCO_3$ in our operated
639 microfluidic cell configuration. In addition, considering the fact that CO_3^{2-} did not precipitate in the
640 absence of Ca^{2+} , the results in this section corroborated with those in section 4.4.1 in which CO_3^{2-}
641 only underwent precipitation with Ca^{2+} to form $CaCO_3$ deposit. The evolution of modeled interfacial
642 CO_3^{2-} concentration in the case without Ca^{2+} plotted in **Figs. 7(c)** and **7(d)** might as well come into
643 similar conclusion. Interfacial CO_3^{2-} concentration increased in conjunction to OH^- production on
644 electrode surface. No CO_3^{2-} was consumed at the vicinity of cathode in the absence of Ca^{2+} allowing
645 a continuous and quicker shift into CO_3^{2-} form at cathode interface. The interfacial CO_3^{2-}
646 concentration arrived at a quasi-plateau at the end of electrolysis when the majority of carbon was

647 converted into CO_3^{2-} form. Slower rate of OH^- production at higher applied current was due to
648 involvement of H_2 evolution activity.

649 To summarize, Mg^{2+} deposited under the form of $\text{Mg}(\text{OH})_2$ and it was not influenced by the presence
650 of Ca^{2+} nor CO_3^{2-} . Only applied current density influenced the electro-precipitation of $\text{Mg}(\text{OH})_2$ as
651 already described in section 4.4.1. According to Bénézeth et al. [52], MgCO_3 or commonly known as
652 magnesite, possesses very slow kinetics of crystallization. Other hydrated Mg-carbonates forms are
653 plausible owing to slow precipitation kinetics of the former, but they are rather unstable due to strong
654 hydrated character of Mg^{2+} [52, 86, 87]. As a result, direct electro-precipitation of MgCO_3 would be
655 realizable but only under stringent conditions, i.e. elevated departing supersaturated solution, elevated
656 temperature and very high CO_2 partial pressure [88]. Hence, based on our experimental results
657 supported by the work of other authors, MgCO_3 was not formed under our experimental conditions.



658

659 **Fig. 7.** Evolution of Mg²⁺ (**a, b**) and modeled interfacial CO₃²⁻ (**c, d**) concentrations during the
 660 electrolysis of electrolyte containing Ca²⁺ (■, □) or without Ca²⁺ (×, +) at 4 mA cm⁻² (**a, c**) and 0.4
 661 mA cm⁻² (**b, d**). Model curves of electrolyte in presence of Ca²⁺ (—) or in absence of Ca²⁺ (
 662 — · —). **Inset (a):** zoom of the initial kinetics evolution of Mg²⁺. Anode: BDD, cathode: stainless
 663 steel and inter-electrode distance: 500 μm.

664

665 4.4.4 Evolution of pH and conductivity

666 In **Fig. S3** are plotted the graphs of variation of bulk solution pH and ionic conductivity throughout
667 the electrolysis of all investigated matrices of electrolyte at both high and low applied current
668 densities. Few general trends can be drawn from these curves. Firstly, solution pH and ionic
669 conductivity tended to decrease in the bulk during the electro-precipitation process. The decrease in
670 pH was the most remarkable in the electrolyte without carbonates since no buffer effect of HCO_3^-
671 $/\text{CO}_3^{2-}$ was present in this matrix. Similar remark was also made by other authors, Tlili et al. [64] and
672 Piri et al. [43], when they checked upon the variation of pH in bulk solution during the formation of
673 CaCO_3 . This drop of pH value was ascribed to the consumption of OH^- that partake in the reaction of
674 $\text{Mg}(\text{OH})_2$ deposition according to **Eq. (3)**. It could also be attributed to the pH participation towards
675 the thermodynamic equilibrium shift of $\text{HCO}_3^-/\text{CO}_3^{2-}$ in favor of CO_3^{2-} formation in **Eq. (5)**, while
676 consuming OH^- . Net concentration of OH^- in the bulk therefore declined, indicated by the decrease
677 of measured bulk pH. The only case where bulk pH did not decrease was during the electrolysis of
678 electrolyte in absence of Ca^{2+} . At both applied current densities, CaCO_3 deposit was not formed.
679 Meanwhile, OH^- was continuously electro-generated on the surface of cathode. OH^- diffusing from
680 cathode surface to the bulk only reacted with existing HCO_3^- until complete conversion into the basic
681 form, i.e. CO_3^{2-} (**Eq. (5)**). Then, the accumulation of OH^- in the bulk yielded in an increase of pH
682 value. Moreover, the only electro-precipitation that occurred in the electrolyte in absence of Ca^{2+} was
683 $\text{Mg}(\text{OH})_2$ and it was only seen at higher range of applied current density. However, as demonstrated
684 in **Fig. S3(a)**, OH^- consumed for the deposition of $\text{Mg}(\text{OH})_2$ on cathode surface contributed trivially
685 towards the diminishing pattern of pH in the bulk unlike during the deposition of CaCO_3 .

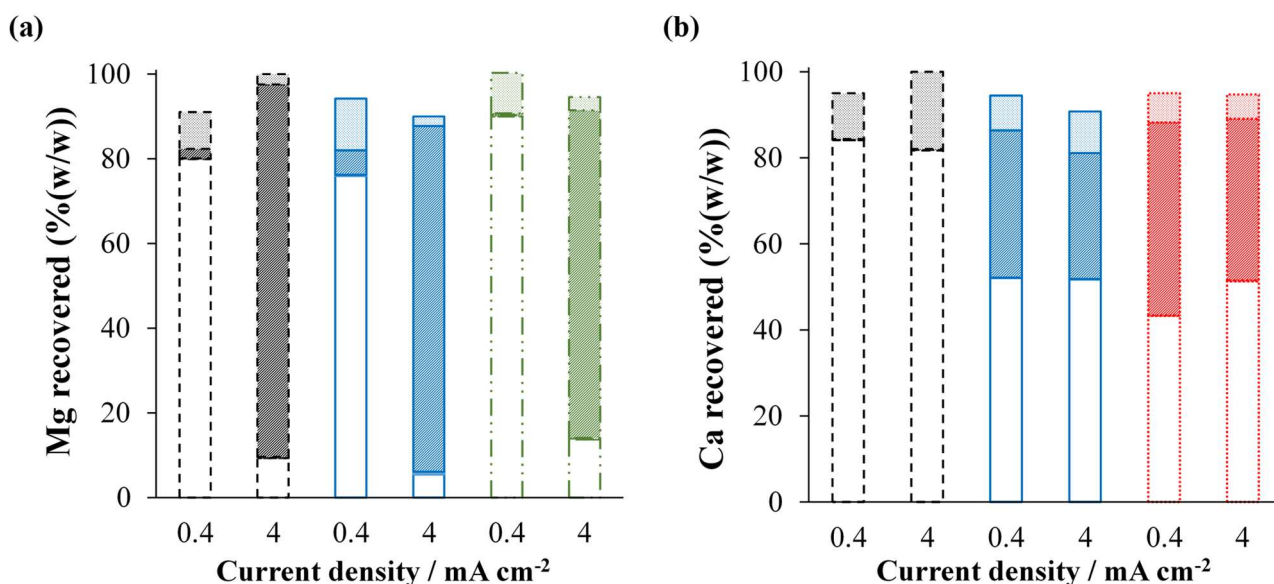
686 Similar argument can be done towards the trend of ionic conductivity in the bulk. Knowing the fact
687 that OH^- possesses high value of ionic conductivity despite not being the highest relatively to H^+ , its
688 consumption throughout the electro-precipitation event of CaCO_3 manifested a decline in overall bulk
689 ionic conductivity as shown in **Fig. S3(c)** and **Fig. S3(d)**.

690 4.4.5 Mass balance and elements recovery

691 **Fig. 8** depicts the recovery of Mg and Ca from the different electrochemical reactor compartments at
692 the end of experiment for different matrices of electrolyte at both current densities investigated. Very
693 high percentage of Mg and Ca recovery across all experiments was verified with the lowest being
694 90%. The percentage of recovery across all electrolysis took an average value of 95%. From **Fig. 8**,
695 in the case where electro-precipitation occurred, high percentage of Mg and Ca were recovered from
696 cathode while negligible quantity was found in tubing and from anode surface. It is important to note
697 that high Mg and Ca recovery means negligible loss of the elements was ensured. Mass balance of
698 Mg and Ca from different compartment was conserved. Consequently, the trends of cation
699 concentrations depicted in previous figures were reliable. Their decay from electrolyte bulk, coupled
700 to high mass recovery from cathode surface was indicative of mineral precipitations occurring on the
701 cathode.

702 Looking at **Fig. 8(b)**, percentages of mass of Ca recovered from cathode in both matrices of
703 electrolyte were higher at 0.4 mA cm^{-2} as compared to 4 mA cm^{-2} , confirming the relative influence
704 of evolving gas activity on cathode surface. Moreover, the percentage of Ca recovery from cathode
705 was always lower in the matrix in presence of Mg^{2+} , whatever the current density applied. It is in
706 agreement with the fact that less Ca^{2+} was electro-precipitated in presence of Mg^{2+} demonstrating the
707 inhibition effect of the latter towards CaCO_3 co-precipitation with $\text{Mg}(\text{OH})_2$.

708 On the other hand, the recovery of Mg in all electrolytes under study illustrated in **Fig. 8(a)** confirmed
709 that the Mg^{2+} -based deposit only took place under high current density. It further corroborated the
710 fact that the formation of $\text{Mg}(\text{OH})_2$ deposit was not influenced by other ionic species co-present in
711 the electrolyte.



712

713 **Fig. 8.** Percentages (w/w) of **(a)** Mg and **(b)** Ca recovered from different parts of experimental pilot
 714 (□: electrolyte, ▨: cathode, ▩: anode and ▩: tube) after 300 min-electrolysis at 0.4 and 4 mA cm⁻²
 715 of different matrices of electrolyte ((- - - -): Ca²⁺ and Mg²⁺ without CO₃²⁻, (—): Ca²⁺, Mg²⁺
 716 and CO₃²⁻, (- · · ·): Ca²⁺ and CO₃²⁻ without Mg²⁺, and (- · · · ·): Mg²⁺ and CO₃²⁻ without Ca²⁺).

717 4.4.6 Theoretical evolution of Ca²⁺, Mg²⁺ and interfacial CO₃²⁻ during electrolysis in different 718 matrices

719 Simulations of evolution of Mg²⁺ concentration during the electrolysis of all matrices of electrolyte
 720 depicted in **Fig. 5(a)**, **Fig. 5(b)**, **Fig. 7(a)** and **Fig. 7(b)** fitted very well with their corresponding
 721 experimental curves. Their RMSE values stayed underneath 0.0078 as summarized in **Table S2** whilst
 722 ME and IOA values remained above 0.9849 and 0.9956 respectively under all case study. The
 723 modelling indicated that under the polarization of 4 mA cm⁻², it took approximately 7 min for the
 724 electrochemical system to reach interfacial OH_{crit}⁻ (0.16 mol m⁻³, interfacial pH_{crit} = 10.2) before Mg²⁺
 725 starting to precipitate. This lag time was also observed experimentally as illustrated in **inset** of **Fig.**
 726 **5(a)** and **Fig. 7(a)**. The model of Mg²⁺ concentrations decreased over time following the calibrated
 727 empirical value of $k_{Mg(OH)_2}$ of 0.330 m⁶ mol⁻² min⁻¹. Exactly same trend was observed across all
 728 matrices of electrolyte containing Mg²⁺ since Mg(OH)₂ deposition was independent of CO₃²⁻ and Ca²⁺

729 ions. Accordingly, similar procedures were carried out for Ca(OH)₂ deposit. However, due to high
730 solubility of Ca(OH)₂, the OH_{crit}^- concentration that needed to be reached was as high as 36.6 mol m⁻³
731 (pH = 12.6). Under our investigated experimental setup, this OH_{crit}^- value was not achieved by either
732 applied current density. Maximum theoretical interfacial OH⁻ concentration was obtained under 4 mA
733 cm⁻² at 7.43 mol m⁻³ (pH = 11.8). As a consequence, no precipitation of Ca(OH)₂ was observed.

734 The modelling of interfacial CO₃²⁻ concentration at cathode surface was rather accurate as extensively
735 discussed in section 4.4.1 to 4.4.3. In agreement to Eq. (20) and Eq. (23), interfacial CO₃²⁻ was proven
736 to be dependent on applied current density; hence H₂ gas evolution activity on cathode. Its
737 concentration was as well influenced by the consumption of interfacial OH⁻. Taking into account
738 these matters, Eq. (21) yields reliable models of evolution of Ca²⁺ concentration across multiple
739 matrices of electrolyte investigated. The calibrated empirical value of constant rate of CaCO₃ electro-
740 precipitation (k_{CaCO_3}) was $3.6 \times 10^{-3} \text{ m}^3 \text{ mol}^{-1} \text{ min}^{-1}$. Ca²⁺ model curves fitted their experimental
741 counterparts well. In agreement to listed values in Table S2, the lowest RMSE was 0.0761 in the
742 system containing Mg²⁺, Ca²⁺ and CO₃²⁻ at low applied current density. Other RMSE values ranged
743 from 0.0828 to 0.1163 and the Ca²⁺ model fitting remained reliable in accordance to other model
744 fitting criteria such as ME and IOA. Their respective values obtained for the case with worst RMSE
745 fitting (i.e. matrix containing Ca²⁺ and CO₃²⁻ without Mg²⁺ at 0.4 mA cm⁻²) were 0.9758 and 0.9934.

746 In order to account for intensive concomitant H₂ gas evolution at high applied current density, the
747 corrective term α introduced in Eq. (10) and Eq. (23) was taken at 7.5% to fit experimental results.
748 This tells that approximately only 7.5% of cathode surface was effective for mineral electro-
749 precipitation including the detachment of deposits already formed by the evolving gas. The α value
750 was found to approximately match the observed experimental decrease of CaCO₃ scaling (7.2%)
751 between the two regions of applied current densities investigated. In addition, it has also been
752 observed that at lower applied current, the applied current density already surpassed limiting current
753 density (section 4.3). This means that secondary reaction like concurrent gas evolution was already

754 present but it did not influence on the availability of interfacial CO_3^{2-} on cathode (**Fig. 6(b)**) but rather
755 improving the mass transport of Ca^{2+} and Mg^{2+} towards cathode surface (section **4.4.1**). The
756 hindrance of CaCO_3 growth kinetics in this case was purely attributed to steric inhibition of Mg^{2+} in
757 solution since no $\text{Mg}(\text{OH})_2$ was produced under this condition [81]. Therefore, the kinetic law of
758 depositing CaCO_3 was slightly modified taking into account this effect as defined in **Eq. (32)**:

$$759 \quad r_{\text{Ca}^{2+}} = -r_{\text{CaCO}_3} = -(k_{\text{CaCO}_3} - k_{\text{inhib}}) [\text{Ca}^{2+}][\text{CO}_3^{2-}]_{\text{int},t} \quad (32)$$

760 where k_{inhib} (in $\text{m}^3 \text{mol}^{-1} \text{min}^{-1}$) is the steric inhibition of Mg^{2+} ion either by adsorption or
761 incorporation into CaCO_3 lattices as previously discussed in section **4.4.2**. By fitting the modeled
762 Ca^{2+} concentration with its experimental data (the matrix in presence of Mg^{2+}) at low applied current
763 density, k_{inhib} was evaluated to be $9.0 \times 10^{-4} \text{m}^3 \text{mol}^{-1} \text{min}^{-1}$. This value is about 25% of the empirical
764 CaCO_3 electro-precipitation constant of k_{CaCO_3} . It suggests that in the presence of 5mg L^{-1} of Mg^{2+}
765 (in the system containing 150mg L^{-1} of Ca^{2+}), 25% less CaCO_3 electro-precipitation should have
766 been observed due to the inhibition effect. However, experimental results indicated only 12% less
767 CaCO_3 scaling after 5 hours of electrolysis, which is about half the theoretical value. This discrepancy
768 was attributed to the enhancement of Ca^{2+} , CO_3^{2-} and Mg^{2+} transport by micro- and macro-convection
769 towards cathode interface [73-76] which could favor the electro-precipitation reactions.

770 **5. Conclusions**

771 The occurrence of mineral electro-precipitation inside a microfluidic reactor was newly investigated
772 in this work. Due to the existence of precipitating agents in water resources of natural or
773 anthropogenic origin, electro-precipitates can be formed during advanced electro-oxidation processes
774 and they might compromise the efficiency of such processes. Inside a scalable microfluidic reactor
775 equipped with BDD, the phenomenon of local alkalization on cathode surface originated principally
776 from reduction of water and not dissolved O_2 under investigated conditions. The reaction kinetics at
777 the proximity of cathode surface were limited by mass transport. Upon further investigation, the

778 influence of electromigration towards the occurrence of electro-precipitation was negligible, meaning
779 that diffusion was the main limiting factor.

780 MgCO_3 deposit was not observed throughout this work, while Mg(OH)_2 precipitate was highly
781 dependent on applied current density, because the local pH value was the decisive parameter upon its
782 formation. Thus Mg(OH)_2 was hardly formed at low applied current density. In addition, Mg(OH)_2
783 deposition was independent of ionic species jointly present in the electrolyte bulk. Regarding Ca-
784 based precipitates, Ca(OH)_2 was not formed under our investigated configuration, while CaCO_3 was
785 easily deposited on the surface of cathode even under small current polarization. More electro-
786 precipitation of CaCO_3 was recovered at lower current density (0.4 mA cm^{-2}) owing to vigorous gas
787 evolution at higher applied current density (4 mA cm^{-2}). CaCO_3 scaling was proven to be impeded by
788 the presence of Mg^{2+} ion. A novel mathematical model was proposed to simulate and predict the
789 evolution of depositing species of Mg^{2+} , Ca^{2+} and interfacial CO_3^{2-} in presence or absence of co-
790 deposition within the microfluidic reactor. The models fitted well with experimental data given the
791 RMSE, ME and IOA values.

792 It could be deduced eventually that $\cdot\text{OH}$ continuously produced on BDD anode did not influence
793 towards the electro-precipitation occurring on cathode counterpart in the applied condition despite
794 micrometric distance separating them. In order to minimize scaling formation, a compromise with
795 respect to degradation efficiency of pollutant needs to be accommodated for upcoming research.
796 Lower applied current density could be used, but lower degradation of pollutant via direct electron
797 transfer or indirect oxidation would be consequently expected due to lower overpotential.
798 Alternatively, mineral electro-precipitation could be minimized by applying high current density,
799 benefiting the intensified evolving gas on cathode surface to un-do the deposits. However, energy
800 consumption would be deemed deal-breaker for its application at industrial scale. Nonetheless, since
801 micrometric range of inter-electrode distance extensively cut down the internal resistance of
802 electrochemical cells, cell voltage would not be eventually so high at such high current densities.

803 Further studies are required to test microfluidic configuration in order to concomitantly yield high
804 degradation efficiency while minimizing the resulting mineral electro-precipitation.

805 **Acknowledgments**

806 Authors would like to express their gratitude to French ministry of higher education and research
807 (MESRI) for financial funding of doctoral contract of Faidzul Hakim Adnan as well as financial
808 support received from Carnot ICEEL, LTSER Zone Atelier du bassin de la Moselle (ZAM) and
809 European regional development fund program (CPER SusChemProc).

- 811 [1] S.D. Richardson, S.Y. Kimura, Water analysis: Emerging contaminants and current issues,
812 Analytical Chemistry, 88 (2016) 546-582.
- 813 [2] B. Petrie, R. Barden, B. Kasprzyk-Hordern, A review on emerging contaminants in wastewaters
814 and the environment: Current knowledge, understudied areas and recommendations for future
815 monitoring, Water Research, 72 (2015) 3-27.
- 816 [3] M.A. Oturan, J.-J. Aaron, Advanced oxidation processes in water/wastewater treatment:
817 Principles and applications. A review, Critical Reviews in Environmental Science and Technology,
818 44 (2014) 2577-2641.
- 819 [4] H. Monteil, Y. Péchaud, N. Oturan, M.A. Oturan, A review on efficiency and cost effectiveness
820 of electro- and bio-electro-fenton processes: Application to the treatment of pharmaceutical pollutants
821 in water, Chemical Engineering Journal, 376 (2019) 119577.
- 822 [5] C.A. Martínez-Huitle, M.A. Rodrigo, I. Sirés, O. Scialdone, Single and coupled electrochemical
823 processes and reactors for the abatement of organic water pollutants: A critical review, Chemical
824 Reviews, 115 (2015) 13362-13407.
- 825 [6] F.C. Moreira, R.A.R. Boaventura, E. Brillas, V.J.P. Vilar, Electrochemical advanced oxidation
826 processes: A review on their application to synthetic and real wastewaters, Applied Catalysis B:
827 Environmental, 202 (2017) 217-261.
- 828 [7] E. Mousset, N. Oturan, M.A. Oturan, An unprecedented route of OH radical reactivity evidenced
829 by an electrocatalytical process: Ipso-substitution with perhalogenocarbon compounds, Applied
830 Catalysis B: Environmental, 226 (2018) 135-146.
- 831 [8] E. Mousset, Y. Pechaud, N. Oturan, M.A. Oturan, Charge transfer/mass transport competition in
832 advanced hybrid electrocatalytic wastewater treatment: Development of a new current efficiency
833 relation, Applied Catalysis B: Environmental, 240 (2019) 102-111.
- 834 [9] P.V. Nidheesh, G. Divyapriya, N. Oturan, C. Trellu, M.A. Oturan, Environmental applications of
835 boron-doped diamond electrodes: 1. Applications in water and wastewater treatment,
836 ChemElectroChem, 6 (2019) 2124-2142.
- 837 [10] O. Scialdone, A. Galia, C. Guarisco, S. Randazzo, G. Filardo, Electrochemical incineration of
838 oxalic acid at boron doped diamond anodes: Role of operative parameters, Electrochimica Acta, 53
839 (2008) 2095-2108.
- 840 [11] O. Scialdone, E. Corrado, A. Galia, I. Sirés, Electrochemical processes in macro and microfluidic
841 cells for the abatement of chloroacetic acid from water, Electrochimica Acta, 132 (2014) 15-24.
- 842 [12] O. Scialdone, A. Galia, S. Sabatino, D. Mira, C. Amatore, Electrochemical conversion of
843 dichloroacetic acid to chloroacetic acid in a microfluidic stack and in a series of microfluidic reactors,
844 ChemElectroChem, 2 (2015) 684-690.
- 845 [13] E. Mousset, Unprecedented reactive electro-mixing reactor: Towards synergy between micro-
846 and macro-reactors?, Electrochemistry Communications, 118 (2020) 106787.
- 847 [14] J.F. Pérez, J. Llanos, C. Sáez, C. López, P. Cañizares, M.A. Rodrigo, Development of an
848 innovative approach for low-impact wastewater treatment: A microfluidic flow-through
849 electrochemical reactor, Chemical Engineering Journal, 351 (2018) 766-772.
- 850 [15] P. Ma, H. Ma, S. Sabatino, A. Galia, O. Scialdone, Electrochemical treatment of real wastewater.
851 Part 1: Effluents with low conductivity, Chemical Engineering Journal, 336 (2018) 133-140.
- 852 [16] E. Mousset, M. Puce, M.N. Pons, Advanced electro-oxidation with boron-doped diamond for
853 acetaminophen removal from real wastewater in a microfluidic reactor: Kinetics and mass-transfer
854 studies, ChemElectroChem, 6 (2019) 2908-2916.
- 855 [17] F. Sopaj, N. Oturan, J. Pinson, F. Podvorica, M.A. Oturan, Effect of the anode materials on the
856 efficiency of the electro-fenton process for the mineralization of the antibiotic sulfamethazine,
857 Applied Catalysis B: Environmental, 199 (2016) 331-341.

858 [18] L. Beaunier, C. Gabrielli, G. Poindessous, G. Maurin, R. Rosset, Investigation of electrochemical
859 calcareous scaling: Nuclei counting and morphology, *Journal Of Electroanalytical Chemistry*, 501
860 (2001) 41-53.

861 [19] C. Deslouis, D. Festy, O. Gil, G. Rius, S. Touzain, B. Tribollet, Characterization of calcareous
862 deposits in artificial sea water by impedance techniques — 1. Deposit of CaCO_3 without $\text{Mg}(\text{OH})_2$,
863 *Electrochimica Acta*, 43 (1998) 1891-1901.

864 [20] C. Deslouis, I. Frateur, G. Maurin, B. Tribollet, Interfacial pH measurement during the reduction
865 of dissolved oxygen in a submerged impinging jet cell, *Journal of Applied Electrochemistry*, 27
866 (1997) 482-492.

867 [21] H. Deligianni, L.T. Romankiw, In situ surface pH measurement during electrolysis using a
868 rotating pH electrode, *IBM Journal of Research and Development*, 37 (1993) 85-95.

869 [22] J. Marin-Cruz, R. Cabrera-Sierra, M. Pech-Canul, I. Gonzalez, EIS study on corrosion and scale
870 processes and their inhibition in cooling system media, *Electrochimica Acta*, 51 (2006) 1847-1854.

871 [23] J. Marin-Cruz, E. Garcia-Figueroa, M. Miranda-Hernández, I. Gonzalez, Electrochemical
872 treatments for selective growth of different calcium carbonate allotropic forms on carbon steel, *Water*
873 *Research*, 38 (2004) 173-183.

874 [24] Y. Ben Amor, L. Bousselmi, H. Takenouti, E. Triki, Influence of sulphate ions on corrosion
875 mechanism of carbon steel in calcareous media, *Corrosion Engineering, Science and Technology*, 40
876 (2005) 129-136.

877 [25] Y. Ben Amor, L. Bousselmi, B. Tribollet, E. Triki, Study of the effect of magnesium
878 concentration on the deposit of allotropic forms of calcium carbonate and related carbon steel
879 interface behavior, *Electrochimica Acta*, 55 (2010) 4820-4826.

880 [26] L. Bousselmi, C. Fiaud, B. Tribollet, E. Triki, Impedance spectroscopic study of a steel electrode
881 in condition of scaling and corrosion: Interphase model, *Electrochimica Acta*, 44 (1999) 4357-4363.

882 [27] L. Bousselmi, C. Fiaud, B. Tribollet, E. Triki, The characterisation of the coated layer at the
883 interface carbon steel-natural salt water by impedance spectroscopy, *Corrosion Science*, 39 (1997)
884 1711-1724.

885 [28] Z. Belarbi, B. Sotta, L. Makhloufi, B. Tribollet, J. Gamby, Modelling of delay effect of calcium
886 carbonate deposition kinetics on rotating disk electrode in the presence of green inhibitor,
887 *Electrochimica Acta*, 189 (2016) 118-127.

888 [29] M. Euvrad, F. Membrey, C. Filiatre, C. Pignolet, A. Foissy, Kinetic study of the
889 electrocrystallization of calcium carbonate on metallic substrates, *Journal Of Crystal Growth*, 291
890 (2006) 428-435.

891 [30] C. Deslouis, D. Festy, O. Gil, V. Maillot, S. Touzain, B. Tribollet, Characterization of calcareous
892 deposits in artificial sea water by impedances techniques: 2-deposit of $\text{Mg}(\text{OH})_2$ without CaCO_3 ,
893 *Electrochimica Acta*, 45 (2000) 1837-1845.

894 [31] R. Jaouhari, A. Benbachir, A. Guenbour, C. Gabrielli, J. Garcia-Jareno, G. Maurin, Influence of
895 water composition and substrate on electrochemical scaling, *Journal of The Electrochemical Society*,
896 147 (2000) 2151.

897 [32] A. Martinod, A. Neville, M. Euvrad, K. Sorbie, Electrodeposition of a calcareous layer: Effects
898 of green inhibitors, *Chemical Engineering Science*, 64 (2009) 2413-2421.

899 [33] C. Deslouis, P. Falaras, O. Gil, M. Jeannin, V. Maillot, B. Tribollet, Influence of clay on
900 calcareous deposit in natural and artificial sea water, *Electrochimica Acta*, 51 (2006) 3173-3180.

901 [34] S.-H. Lin, S.C. Dexter, Effects of temperature and magnesium ions on calcareous deposition,
902 *Corrosion*, 44 (1988) 615-622.

903 [35] J. Marin-Cruz, R. Cabrera-Sierra, M. Pech-Canul, I. Gonzalez, Characterization of different
904 allotropic forms of calcium carbonate scales on carbon steel by electrochemical impedance
905 spectroscopy, *Journal of Applied Electrochemistry*, 34 (2004) 337-343.

906 [36] S.M. Hoseinie, T. Shahrabi, Influence of ionic species on scaling and corrosion performance of
907 AISI 316L rotating disk electrodes in artificial seawater, *Desalination*, 409 (2017) 32-46.

908 [37] S.M. Hoseinie, T. Shahrabi, B. Ramezanzadeh, M.F. Rad, The role of porosity and surface
909 morphology of calcium carbonate deposits on the corrosion behavior of unprotected API 5L X52

910 rotating disk electrodes in artificial seawater, *Journal of The Electrochemical Society*, 163 (2016)
911 C515-C529.

912 [38] F. Sopaj, N. Oturan, J. Pinson, F.I. Podvorica, M.A. Oturan, Effect of cathode material on electro-
913 fenton process efficiency for electrocatalytic mineralization of the antibiotic sulfamethazine,
914 *Chemical Engineering Journal*, 384 (2020) 123249.

915 [39] S. Mathé, *Chimie des solutions*, Dunod2018.

916 [40] W.M. Haynes, *CRC Handbook of chemistry and physics*, 97th ed., CRC press, 2017.

917 [41] H. Vogt, R.J. Balzer, The bubble coverage of gas-evolving electrodes in stagnant electrolytes,
918 *Electrochimica Acta*, 50 (2005) 2073-2079.

919 [42] C. Barchiche, C. Deslouis, D. Festy, O. Gil, P. Refait, S. Touzain, B. Tribollet, Characterization
920 of calcareous deposits in artificial seawater by impedance techniques: 3 — deposit of CaCO₃ in the
921 presence of Mg(II), *Electrochimica Acta*, 48 (2003) 1645-1654.

922 [43] M. Piri, R. Arefinia, Investigation of the hydrogen evolution phenomenon on CaCO₃
923 precipitation in artificial seawater, *Desalination*, 444 (2018) 142-150.

924 [44] O. Scialdone, A. Galia, S. Sabatino, Electro-generation of H₂O₂ and abatement of organic
925 pollutant in water by an electro-fenton process in a microfluidic reactor, *Electrochemistry*
926 *Communications*, 26 (2013) 45-47.

927 [45] J. Newman, K.E. Thomas-Alyea, *Electrochemical systems*, 3rd ed., John Wiley & Sons, 2012.

928 [46] O. Velts, M. Uibu, J. Kallas, R. Kuusik, CO₂ mineral trapping: Modeling of calcium carbonate
929 precipitation in a semi-batch reactor, *Energy Procedia*, 4 (2011) 771-778.

930 [47] S.J. Kakaraniya, A. Mehra, Reactive precipitation in gas-liquid systems, *Industrial &*
931 *Engineering Chemistry Research*, 46 (2007) 1125-1137.

932 [48] C. Kazadi Mbamba, D.J. Batstone, X. Flores-Alsina, S. Tait, A generalised chemical
933 precipitation modelling approach in wastewater treatment applied to calcite, *Water Research*, 68
934 (2015) 342-353.

935 [49] Y. Zhang, R.A. Dawe, Influence of Mg²⁺ on the kinetics of calcite precipitation and calcite
936 crystal morphology, *Chemical Geology*, 163 (2000) 129-138.

937 [50] M. Ben Amor, D. Zgolli, M.M. Tlili, A.S. Manzola, Influence of water hardness, substrate nature
938 and temperature on heterogeneous calcium carbonate nucleation, *Desalination*, 166 (2004) 79-84.

939 [51] J.N. Butler, *Carbon dioxide equilibria and their applications*, 1st ed., Taylor & Francis Group,
940 New York: Routledge, 1991.

941 [52] P. Bénézech, G.D. Saldi, J.-L. Dandurand, J. Schott, Experimental determination of the solubility
942 product of magnesite at 50 to 200°C, *Chemical Geology*, 286 (2011) 21-31.

943 [53] P. Reichert, AQUASIM - a tool for simulation and data analysis of aquatic systems, *Water*
944 *Science and Technology*, 30 (1994) 21.

945 [54] E. Mousset, S. Pontvianne, M.-N. Pons, Fate of inorganic nitrogen species under homogeneous
946 fenton combined with electro-oxidation/reduction treatments in synthetic solutions and reclaimed
947 municipal wastewater, *Chemosphere*, 201 (2018) 6-12.

948 [55] C.A. Martínez-Huitle, M. Panizza, Electrochemical oxidation of organic pollutants for
949 wastewater treatment, *Current Opinion in Electrochemistry*, 11 (2018) 62-71.

950 [56] E. Mousset, L. Quackenbush, C. Schondek, A. Gerardin-Vergne, S. Pontvianne, S. Kmiotek, M.-
951 N. Pons, Effect of homogeneous Fenton combined with electron transfer on the fate of inorganic
952 chlorinated species in synthetic and reclaimed municipal wastewater, *Electrochimica Acta*, 334
953 (2020) 135608.

954 [57] E. Mousset, D.D. Dionysiou, Photoelectrochemical reactors for treatment of water and
955 wastewater: a review, *Environmental Chemistry Letters*, 18 (2020) 1301-1318.

956 [58] N. Vatistas, C. Comninellis, The persulfate process for the mediated oxidation of organic
957 pollutants, in: C. Comninellis, G. Chen (Eds.) *Electrochemistry for the Environment*, Springer New
958 York, New York, NY, 2010, pp. 229-244.

959 [59] B.P. Chaplin, Critical review of electrochemical advanced oxidation processes for water
960 treatment applications, *Environmental Science: Processes & Impacts*, 16 (2014) 1182-1203.

- 961 [60] B.P. Chaplin, Chapter 17 - Advantages, disadvantages, and future challenges of the use of
962 electrochemical technologies for water and wastewater treatment, in: C.A. Martínez-Huitle, M.A.
963 Rodrigo, O. Scialdone (Eds.) *Electrochemical Water and Wastewater Treatment*, Butterworth-
964 Heinemann, 2018, pp. 451-494.
- 965 [61] A.R. Despić, Deposition and dissolution of metals and alloys. Part B: Mechanisms, kinetics,
966 texture, and morphology, in: B.E. Conway, J.O.M. Bockris, E. Yeager, S.U.M. Khan, R.E. White
967 (Eds.) *Comprehensive Treatise of Electrochemistry: Volume 7 Kinetics and Mechanisms of Electrode*
968 *Processes*, Springer US, Boston, MA, 1983, pp. 451-528.
- 969 [62] H. Karoui, B. Riffault, M. Jeannin, A. Kahoul, O. Gil, M. Ben Amor, M.M. Tlili, Electrochemical
970 scaling of stainless steel in artificial seawater: Role of experimental conditions on CaCO₃ and
971 Mg(OH)₂ formation, *Desalination*, 311 (2013) 234-240.
- 972 [63] A.J. Bard, L.R. Faulkner, *Electrochemical methods: Fundamentals and applications*, John Wiley
973 & Sons 2001.
- 974 [64] M.M. Tlili, M. Benamor, C. Gabrielli, H. Perrot, B. Tribollet, Influence of the interfacial pH on
975 electrochemical CaCO₃ precipitation, *Journal of The Electrochemical Society*, 150 (2003) C765.
- 976 [65] S. Sarkar, W. Aquino, Electroneutrality and ionic interactions in the modeling of mass transport
977 in dilute electrochemical systems, *Electrochimica Acta*, 56 (2011) 8969-8978.
- 978 [66] T. Li, T.C. Keener, L. Cheng, Carbon dioxide removal by using Mg(OH)₂ in a bubble column:
979 Effects of various operating parameters, *International Journal of Greenhouse Gas Control*, 31 (2014)
980 67-76.
- 981 [67] M. Panizza, P.A. Michaud, G. Cerisola, C. Comninellis, Anodic oxidation of 2-naphthol at
982 boron-doped diamond electrodes, *Journal Of Electroanalytical Chemistry*, 507 (2001) 206-214.
- 983 [68] P. Cañizares, J. García-Gómez, I. Fernández de Marcos, M.A. Rodrigo, J. Lobato, Measurement
984 of mass-transfer coefficients by an electrochemical technique, *Journal Of Chemical Education*, 83
985 (2006) 1204.
- 986 [69] R.A.W. Dryfe, 20 - Liquid junction potentials, in: C.G. Zoski (Ed.) *Handbook of*
987 *Electrochemistry*, Elsevier, Amsterdam, 2007, pp. 849-877.
- 988 [70] C. Barchiche, C. Deslouis, O. Gil, P. Refait, B. Tribollet, Characterisation of calcareous deposits
989 by electrochemical methods: Role of sulphates, calcium concentration and temperature,
990 *Electrochimica Acta*, 49 (2004) 2833-2839.
- 991 [71] T. Okstad, Ø. Rannestad, R. Johnsen, K. Nisancioglu, Significance of hydrogen evolution during
992 cathodic protection of carbon steel in seawater, *Corrosion*, 63 (2007) 857-865.
- 993 [72] C. Arkam, Quartz crystal electrogravimetry with controlled hydrodynamics, *Journal of The*
994 *Electrochemical Society*, 141 (1994) L103.
- 995 [73] H. Vogt, The role of single-phase free convection in mass transfer at gas evolving electrodes —
996 1. Theoretical, *Electrochimica Acta*, 38 (1993) 1421-1426.
- 997 [74] H. Vogt, Gas-evolving electrodes, in: E. Yeager, J.O.M. Bockris, B.E. Conway, S. Sarangapani
998 (Eds.) *Comprehensive Treatise of Electrochemistry: Electrode Processes: Transport*, Springer US, Boston,
999 MA, 1983, pp. 445-489.
- 1000 [75] L.J.J. Janssen, Behaviour of and mass transfer at gas-evolving electrodes, *Electrochimica Acta*,
1001 34 (1989) 161-169.
- 1002 [76] M.G. Fouad, G.H. Sedahmed, Mass transfer at gas evolving screen electrodes, *Electrochimica*
1003 *Acta*, 20 (1975) 615-618.
- 1004 [77] C. Gabrielli, G. Maurin, G. Poindessous, R. Rosset, Nucleation and growth of calcium carbonate
1005 by an electrochemical scaling process, *Journal Of Crystal Growth*, 200 (1999) 236-250.
- 1006 [78] Y. Ben Amor, L. Bousselmi, M.C. Bernard, B. Tribollet, Nucleation-growth process of calcium
1007 carbonate electrodeposition in artificial water — influence of the sulfate ions, *Journal Of Crystal*
1008 *Growth*, 320 (2011) 69-77.
- 1009 [79] T. Chen, A. Neville, M. Yuan, Calcium carbonate scale formation — assessing the initial stages
1010 of precipitation and deposition, *Journal of Petroleum Science and Engineering*, 46 (2005) 185-194.
- 1011 [80] M. Kitamura, Crystallization and transformation mechanism of calcium carbonate polymorphs
1012 and the effect of magnesium ion, *Journal Of Colloid And Interface Science*, 236 (2001) 318-327.

- 1013 [81] K.E. Mantel, W.H. Hartt, T.-Y. Chen, Substrate, surface finish, and flow rate influences on
1014 calcareous deposit structure, *Corrosion*, 48 (1992) 489-500.
- 1015 [82] C. Gabrielli, Quartz crystal microbalance investigation of electrochemical calcium carbonate
1016 scaling, *Journal of The Electrochemical Society*, 145 (1998) 2386.
- 1017 [83] S. Xu, Structure and morphology of electrodeposited CaCO₃: X-ray diffraction and microscopy
1018 studies, *Journal of The Electrochemical Society*, 146 (1999) 3315.
- 1019 [84] C. Gabrielli, M. Keddam, A. Khalil, R. Rosset, M. Zidoune, Study of calcium carbonate scales
1020 by electrochemical impedance spectroscopy, *Electrochimica Acta*, 42 (1997) 1207-1218.
- 1021 [85] H.J. Meyer, The influence of impurities on the growth rate of calcite, *Journal Of Crystal Growth*,
1022 66 (1984) 639-646.
- 1023 [86] F.L. Sayles, W.S. Fyfe, The crystallization of magnesite from aqueous solution, *Geochimica et*
1024 *Cosmochimica Acta*, 37 (1973) 87-99.
- 1025 [87] L. Hopkinson, K. Rutt, G. Cressey, The transformation of nesquehonite to hydromagnesite in
1026 the system CaO-MgO-H₂O-CO₂: An experimental spectroscopic study, *The Journal of Geology*, 116
1027 (2008) 387-400.
- 1028 [88] M. Hänchen, V. Prigiobbe, R. Baciocchi, M. Mazzotti, Precipitation in the Mg-carbonate system
1029 — effects of temperature and CO₂ pressure, *Chemical Engineering Science*, 63 (2008) 1012-1028.

1030